Geophysical Journal International

Geophys. J. Int. (2011) **184,** 575–594 doi: 10.1111/j.1365-246X.2010.04881.x

The crustal structure of the north-eastern Gulf of Aden continental margin: insights from wide-angle seismic data

L. Watremez,[1,*] S. Leroy,[1,2] S. Rouzo,[1] E. d'Acremont,[1] P. Unternehr,[3] C. Ebinger,[4] F. Lucazeau[5] and A. Al-Lazki[6]

[1] *ISTeP, UPMC University Paris* 06, 75252 *Paris Cedex* 05, *France. E-mail: louise.watremez@upmc.fr*
[2] *ISTeP, CNRS - UMR* 7193, *France*
[3] *Total, Exploration-Production, Geosciences, Paris La Defense* 92078, *France*
[4] *Department Earth and Environmental Sciences, University of Rochester, USA*
[5] *Geosciences Marines, IPGP-CNRS,* 4 *place Jussieu, Paris Cedex* 05 75252, *France*
[6] *University Sultan Qaboos,* PO Box 50, *Al-Khod, Muscat,* PC123, *Oman*

Accepted 2010 November 2. Received 2010 October 28; in original form 2010 March 31

SUMMARY

The wide-angle seismic (WAS) and gravity data of the Encens survey allow us to determine the deep crustal structure of the north-eastern Gulf of Aden non-volcanic passive margin. The Gulf of Aden is a young oceanic basin that began to open at least 17.6 Ma ago. Its current geometry shows first- and second-order segmentation: our study focusses on the Ashawq–Salalah second-order segment, between Alula–Fartak and Socotra–Hadbeen fracture zones. Modelling of the WAS and gravity data (three profiles across and three along the margin) gives insights into the first- and second-order structures. (1) Continental thinning is abrupt (15–20 km thinning across 50–100 km distance). It is accommodated by several tilted blocks. (2) The ocean–continent transition (OCT) is narrow (15 km wide). The velocity modelling provides indications on its geometry: oceanic-type upper-crust (4.5 km s^{-1}) and continental-type lower crust (>6.5 km s^{-1}). (3) The thickness of the oceanic crust decreases from West (10 km) to the East (5.5 km). This pattern is probably linked to a variation of magma supply along the nascent slow-spreading ridge axis. (4) A 5 km thick intermediate velocity body (7.6 to 7.8 km s^{-1}) exists at the crust-mantle interface below the thinned margin, the OCT and the oceanic crust. We interpret it as an underplated mafic body, or partly intruded mafic material emplaced during a 'post-rift' event, according to the presence of a young volcano evidenced by heat-flow measurement (Encens-Flux survey) and multichannel seismic reflection (Encens survey). We propose that the non-volcanic passive margin is affected by post-rift volcanism suggesting that post-rift melting anomalies may influence the late evolution of non-volcanic passive margins.

Key words: Controlled source seismology; Continental margins: divergent; Crustal structure; Indian Ocean.

1 INTRODUCTION

Continental break-up is an important process in forming a new plate boundary. It proceeds by continental extension associated with magmatism and/or tectonic deformation and it leads to continental margins formation and oceanic spreading. Many fundamental questions remain unsolved about the way the lithosphere evolves during the continental rifting and the effects on rift evolution of key parameters such as crustal thickness, composition, extension rate and temperature.

Continental extension begins with extensional stresses applied to the lithosphere until it breaks apart, culminating in crustal rupture and accretion of the new oceanic lithosphere. Continental break-up is a complex process distributed in time and space (Péron-Pinvidic & Manatschal 2009). Realistic rheologies, inducing depth-dependent stretching and focussing of the deformation, have been suggested to explain the evolution of the deformation during extension of the continental lithosphere (e.g. Brun & Beslier 1996; Davis & Kusznir 2004; Lavier & Manatschal 2006; Pérez-Gussinyé *et al.* 2003; Reston 2007; Huismans & Beaumont 2008).

Continental rifted margins are usually classified into volcanic and non-volcanic margins:

(1) Non-volcanic margins are characterized by a block-faulted basement, no clear evidence of magmatism during the rifting and

*Now at: Department of Oceanography, Dalhousie University, Halifax, NS, Canada, B3H 4J1.

a transition between the thinned continental crust and the oceanic crust (ocean–continent transition, OCT, e.g. Chian *et al.* 1995; Dean *et al.* 2000; Funck *et al.* 2003) of variable width (30 to 200 km) and ambiguous nature. A high seismic velocity structure can be observed in the OCT. On the West Iberia margin, drillings, dives and dredges have revealed serpentinised peridotites of a zone of exhumed continental mantle. The OCT have been also interpreted as serpentinised peridotite in the Labrador sea (Chian *et al.* 1995) and the Newfoundland margins (Reid 1994). The limited magmatism of these non volcanic margins has been attributed to ultra-slow opening rates and cold mantle conditions (i.e. ragged oceanic crust, Cannat *et al.* 1995).

(2) Volcanic margins are mostly characterized by seaward dipping reflectors (SDRs) related to tilted basalt floods (e.g. Mutter *et al.* 1982; Geoffroy 2005), a thick lower crust featuring a higher than normal velocity sometimes called underplating and a thick oceanic crust, (e.g. White & McKenzie 1989; Holbrook *et al.* 1994b). The very sharp transition between continental and oceanic domains occur below the SDRs (e.g. Mjelde *et al.* 2005, 2007) and some authors talk about a continent–ocean boundary (COB, e.g. Bauer *et al.* 2000; Hopper *et al.* 2003). Normal faults are observed on volcanic margins, but there is no well-organized tilted blocks (e.g. Veevers & Cotterill 1978; Menzies *et al.* 2002). The excess of melt leading to the large amount of effusive and igneous material at the COB and early oceanic crust is primarily related to a high mantle temperature anomaly (Bown & White 1994; White & McKenzie 1989; Holbrook *et al.* 2001).

Thus, the volcanic or non-volcanic character of a passive margin may be inferred by the OCT nature and crustal thicknesses. Multi-channel seismic (MCS) provides information on superficial structures whereas wide-angle seismic (WAS) and gravity provide crustal thicknesses and indirect information on the OCT nature. Combining these two sets of data allows a good knowledge on the structures and evolution of rifted margins and the location and suggested nature of the OCT (e.g. Horsefield *et al.* 1994; Holbrook *et al.* 1994a,b; Chian *et al.* 1995; Hopper *et al.* 2003; Funck *et al.* 2004; Greenroyd *et al.* 2008). The accurate boundary location of the OCT and its nature are still discussed in areas where there are no samples, such as in the north-eastern Gulf of Aden.

Three second-order segments are described between Alula–Fartak and Socotra–Hadbeen fracture zones (Fig. 1), with different geometries (Fig. 2, Leroy *et al.* 2010b). This WAS/gravity study, coincident with MCS data, focusses on the western second-order segment: Ashawq–Salalah segment to image the structures formed during the rift. The velocity models show the great variability of the crustal structures of the Ashawq–Salalah segment up to the western edge of the Taqah one. Magmatism is evidenced below the OCT and oceanic crusts, suggesting a post-rift magmatic activity of the margin, in agreement with the MCS study (Autin *et al.* 2010).

2 GEOLOGICAL SETTINGS OF THE GULF OF ADEN

The Gulf of Aden is a young oceanic basin which separates Arabia from Somalia (Fig. 1). It exhibits volcanic margins in the western part (Tard *et al.* 1991) related to the Afar hotspot activity and magma-poor margins in the eastern part (d'Acremont *et al.* 2005). The mean orientation of the Gulf of Aden (N75°E), oblique to the

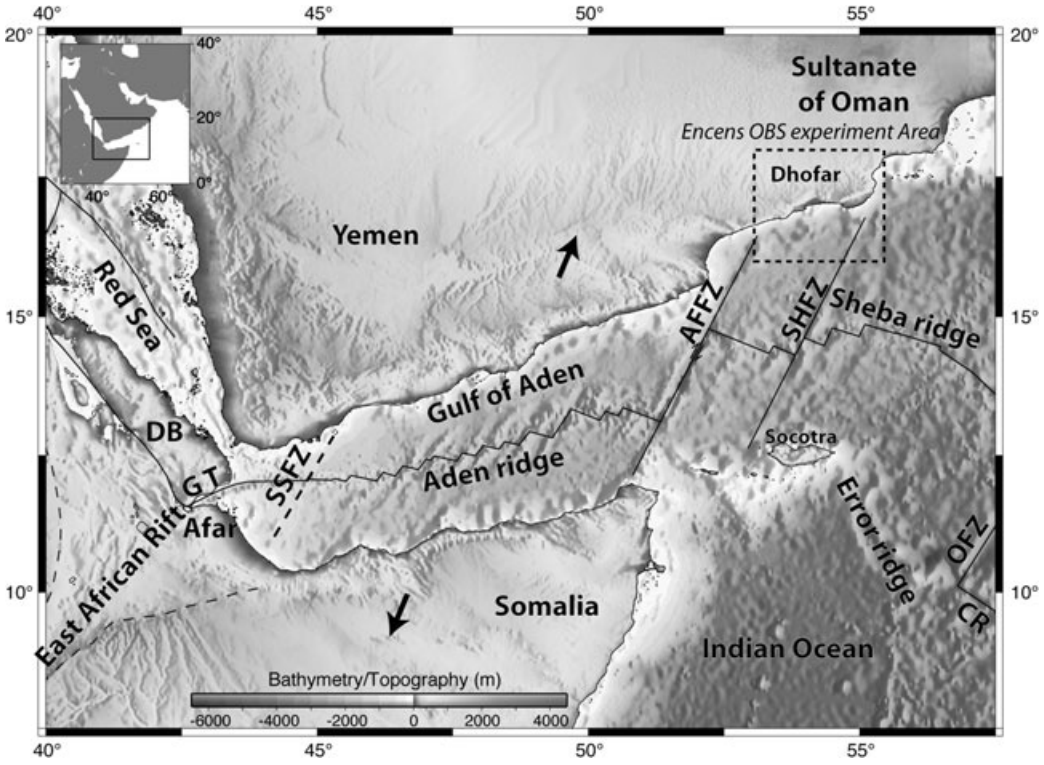

Figure 1. Location of the study area in the eastern Gulf of Aden. AFFZ, Alula–Fartak fracture zone; CR, Carlsberg ridge; DB, Danakil Block; GT, Gulf of Tadjoura; OFZ, Owen fault zone; SHFZ, Socotra-Hadbeen fracture zone; SSFZ, Shukra-el-Sheik fracture zone. The direction of extension of the Gulf is highlighted by the black arrows, full extension velocity in the eastern part of the Gulf of Aden is about 2.34 cm yr^{-1} (Jestin *et al.* 1994), and coastlines and oceanic spreading axis are underlined by continuous lines. Relief is compiled from SRTM topography data (Rodriguez *et al.* 2005) and Sandwell & Smith (1997) predicted bathymetry.

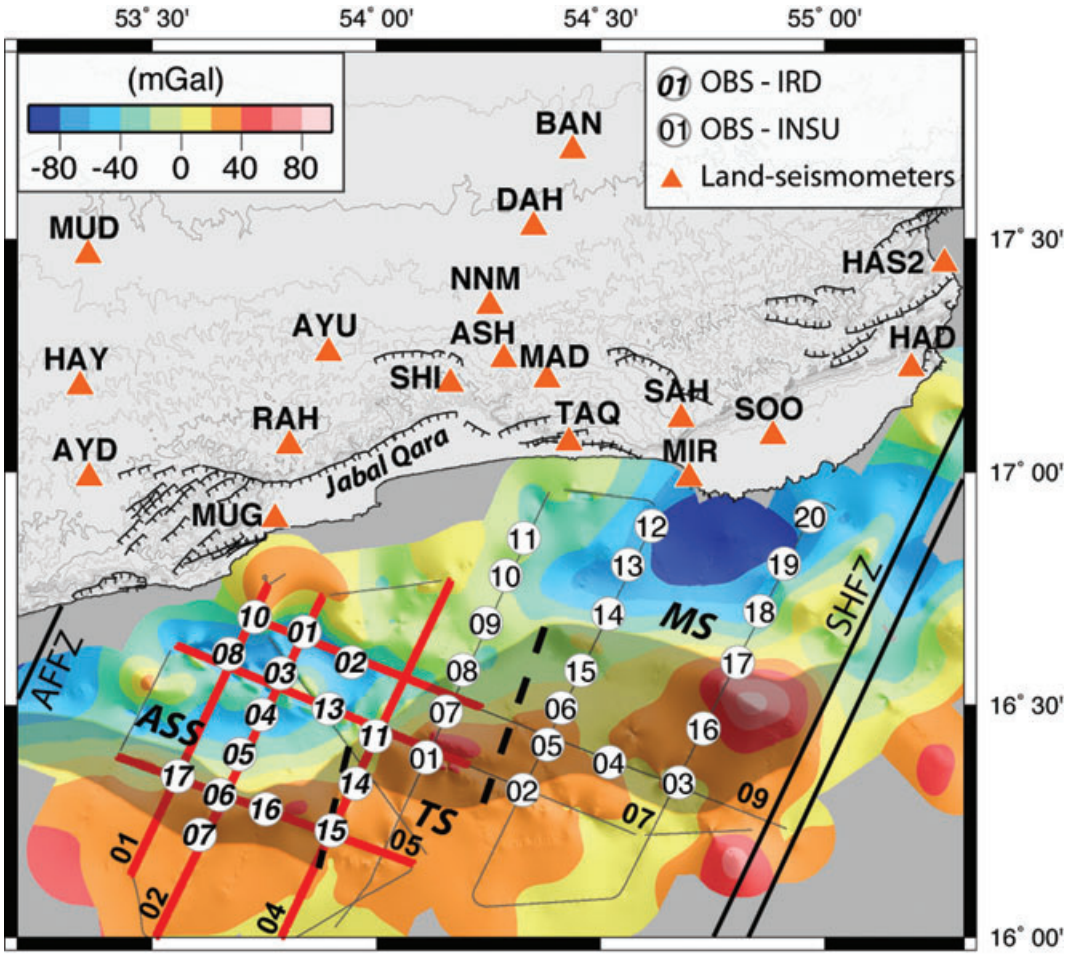

Figure 2. Free-air gravity anomaly map on the Oman margin with locations of OBS, land-stations and wide-angle seismic lines during the Encens experiment. Gravity data are 100 m gridded from the Encens-Sheba and Encens experiments (Leroy *et al.* 2004, 2010b). Grey lines are wide-angle ship track; seismic lines shown in this study are located by red bold lines. AFFZ, Alula–Fartak fracture zone; SHFZ, Socotra–Hadbeen fracture zone; ASS, Ashawq–Salalah segment; TS, Taqah segment; MS, Mirbat segment. Bold dashed lines are segments boundary. Location of the map is shown as a dashed rectangle on the regional map, Fig. 1. Shaded area is OCT inferred from the compilation of geophysical observations (for the Ashawq–Salalah segment; multi-channel/wide-angle seismics, magnetism and heat flow, Autin *et al.* 2010; Leroy *et al.* 2010b). OBS were provided by IRD and INSU institutions. IRD ones (thick numbers) were four components (geophone, vertical and two horizontals) and INSU were two components (geophone and vertical).

direction of extension is N26°E induces a high segmentation of the margins.

Between the Gulf of Tadjoura and the Owen fracture zone, the spreading axis, named Sheba ridge then Aden ridge, is segmented by three main fracture zones, namely the Shukra-el–Sheik fracture zone, the Alula–Fartak and the Socotra–Hadbeen transform faults (Fig. 1). Spreading rates increase from West, close to the Shukra-el-Sheik discontinuity (1.6 cm yr^{-1}, azimuth N025°E), to East between Alula–Fartak and Socotra–Hadbeen fracture zones (2.34 cm yr^{-1} azimuth N027° E; Fournier *et al.* 2001; Vigny *et al.* 2006).

The rifting which started 35 Ma ago (Roger *et al.* 1989; Bott *et al.* 1992; Watchorn *et al.* 1998), coincides with the climax of the Afar hotspot activity (Hofmann *et al.* 1997; Ebinger & Sleep 1998; Kenea *et al.* 2001; Leroy *et al.* 2010a) and the onset of the seafloor spreading occurred at least 17.6 Ma ago in the eastern part (Leroy *et al.* 2004; d'Acremont *et al.* 2006; Leroy *et al.* 2010b). Previous studies of the eastern Gulf of Aden, between Alula–Fartak and Socotra–Hadbeen fracture zones, show that the passive margins are non-volcanic (no SDRs are observed) and outcrops on land (in Southern Oman in Dhofar and Socotra, Roger *et al.* 1989; d'Acremont *et al.* 2005; Bellahsen *et al.* 2006; Autin *et al.* 2010; Leroy *et al.* 2010b, Fig. 1).

The north-eastern Gulf of Aden OCT inferred from seismic reflection data and magnetic and gravity data has been accurately remapped with the new data set of MCS, WAS, gravity, magnetism and heat flow measurements recorded during the Encens and Encens-Flux cruises (Leroy *et al.* 2010b). The OCT is relatively narrow (<15 km wide) in the Ashawq–Salalah segment (Autin *et al.* 2010) and widen toward the east in the Taqah (from 15 to 50 km) and Mirbat segment (50 km, Leroy *et al.* 2010b) and is characterized continentward by the last occurrence of syn-rift wedges of sediments, by a lowering of the free-air gravity anomaly continentward (Fig. 2), by a generally quiet magnetic zone with local anomalies, and by the oldest identified oceanic magnetic anomaly, oceanward. Autin *et al.* (2010) show that the formation of the OCT on this segment of the margin is the result of a long and complex interaction of tectono-metamorphic and magmatic events.

Crustal thicknesses of the Dhofar margin inferred offshore from gravity and onshore from receiver function analysis, ranges from 36.6 km in the North and 25.6 km on the coastline to 16 km and less

to 2 km in the deep part of the north-eastern Gulf of Aden (Leroy *et al.* 2004; d'Acremont *et al.* 2006; Tiberi *et al.* 2007). Crustal thinning is accommodated by several tilted blocks (d'Acremont *et al.* 2005; Autin *et al.* 2010; Leroy *et al.* 2010b) and on land, a thinning of about 11 km occurs in 30 km.

In the Ashawq–Salalah segment, a deep offshore volcano was discovered by heat-flow values as high as 890 mW m^{-2} (Lucazeau *et al.* 2009) on the top of a volcano, imaged by MCS (Autin *et al.* 2010). The study of MCS profiles suggests that the volcano was active after the continental break-up, during the post-rift (Autin *et al.* 2010) and at least until 100 000 yr ago (Lucazeau *et al.* 2009). The late volcanic activity is proposed to be related to a melting anomaly observed in the western segment of the present-day Sheba ridge (d'Acremont *et al.* 2010) and explained by the channelized flow of Afar plume material along the Aden–Sheba ridges system (Leroy *et al.* 2010a). These observations and the evidence of the presence of molten upper-mantle beneath the Dhofar (Basuyau *et al.* 2010) tend to extend the influence of the Afar plume farther eastward into the Gulf of Aden than believed by previous studies (e.g. Hébert *et al.* 2001).

3 DATA ACQUISITION AND MODELLING PROCEDURE

3.1 Encens cruise

One of the two part of the Encens cruise was dedicated to the WAS (Leroy *et al.* 2006). A total of 35 OBS and 21 land-seismometers recording *ca*. 8000 shots were deployed along six profiles parallel and perpendicular to the direction of opening (Fig. 2). The mean distance between OBS is 15 km. OBS data are corrected for the clock drift during the deployment and positions are relocated to correct the possible drift during deployment through inversion of the direct waves arrival times.

The source consists of an array of 18 airguns (seven Bolts and 11 G-guns) of variable volume (1.2 to 16 l, setting a total volume of 138, l at immersion depth of 22–25 m) tuned so that the second bubble pulse of each gun is synchronized, providing a powerful low-frequency source ('monobulle' source, Avedik *et al.* 1993). The shot interval is set to 150 m using differential GPS positioning (approximately 1 min at a speed of 5 knots). Shots were only fired offshore (Fig. 2).

The vertical component of the receivers is chosen for this analysis. Records are of very good quality (e.g. Fig. 3) and no particular processing is required except an offset-dependant gain. A few land-seismometers needed a gentle band-pass filtering to remove low frequency noise. Distinct seismic events are identified at offsets up to 80 km (OBS) and 210 km (landstations).

3.2 Velocity modelling

The 2-D ray tracing algorithm Rayinvr (Zelt & Smith 1992) is used to model the wide-angle seismic data. The model consists in a succession of layers of similar velocities (model parameters are velocity and interface nodes). Traveltimes of the *P*-waves are picked on records as a set of reflected and refracted phases constraining the different layers (see the correspondence between the seismic phases and the geological units and interfaces in Table 1 and Fig. 3). A forward modelling method is adopted, following a top to bottom layer-stripping strategy (Zelt 1999). The velocity model is built layer after layer, with a trial and error approach, minimizing the time-gap between observed and synthetic traveltimes. The uncertainty is evaluated for each pick, depending on the signal to noise ratio, following the parameterization of Zelt & Forsyth (1994). A misfit parameter (χ^2) close to 1 warrants that the data are well exploited, with no over-interpretation (Bevington 1969; Zelt 1999). The number of picks, RMS traveltime residuals and χ^2 are listed for each line in Table 2 and for each phases and whole-models in Table A1.

Reinterpretation of the data may be needed during the process. To achieve the simplest model that account for the data, modelling is carried out introducing as few parameters as possible (velocity and interface nodes). However, the sea bottom and, to a lesser extent, the top-basement interfaces were imaged by the coincident MCS profiles, they are thereby described by a larger number of interface nodes. Eventually, 11 phases are identified, constraining up to six geological units (Table 1).

The velocities of the most superficial structures are prescribed by the two-way traveltimes, converted interfaces (mainly the acoustic basement) and the stack velocities inferred from MCS processing (Autin *et al.* 2010).

3.3 Gravity modelling

Gravity data were continuously acquired during the Encens cruise along MCS and/or WAS profiles using a relative gravimeter (KSS31) (Fig. 2, Leroy *et al.* 2010b).

Modelling of the free-air gravity anomaly provides a valuable control on the velocity structure. An empirical velocity-density relationship is used to infer the density model from velocity distribution (Ludwig *et al.* 1970). The contribution to the anomaly of each block of constant density is estimated using the Talwani *et al.* (1959) method, assuming a 2.5D geometry.

4 RESULTS

4.1 Velocity

The interpretation and modelling of the WAS data lead to the velocity models shown in Figs 4 (across-margin lines, i.e. ENCR01, 02 and 04) and 5 (along-margin lines, i.e. ENCR05, 07, 09). Velocities are colour-coded. Note that segments of velocity models interfaces constrained by wide-angle reflections are shown using a thicker black line and surfaces effectively sampled by seismic rays are highlighted using brighter areas (Figs 4 and 5).

The main features of the velocity models are summarized below, according to the major units.

4.1.1 Sedimentary layers

Although sediments have few imprint in the WAS records, two sedimentary layers limited by an interface are discriminated above the basement in the deepest basins. Typical velocities range from 1.6 to 2.5 km s^{-1} in the upper sedimentary layer and reach 4.2 km s^{-1} in the deep basins (ENCR02, Fig. 4). Velocities are uniform along the lines and from profile to profile. Sediments thickness varies from 1 to 2 km. It locally reaches 3 km in the deeper graben (ENCR01 at 57 km and ENCR02 at 52 and 78 km, Fig. 4). The upper layer relies mostly on syn-OCT and post-rift sediments whereas the lower layer, when observed using WAS data, relies on syn-rift sediments in the thinned continental domain (ENCR01 and 02). The second sedimentary layer is the deep infill of basins; it is constrained by wide-angle reflections and refractions. Its top coincides with a major

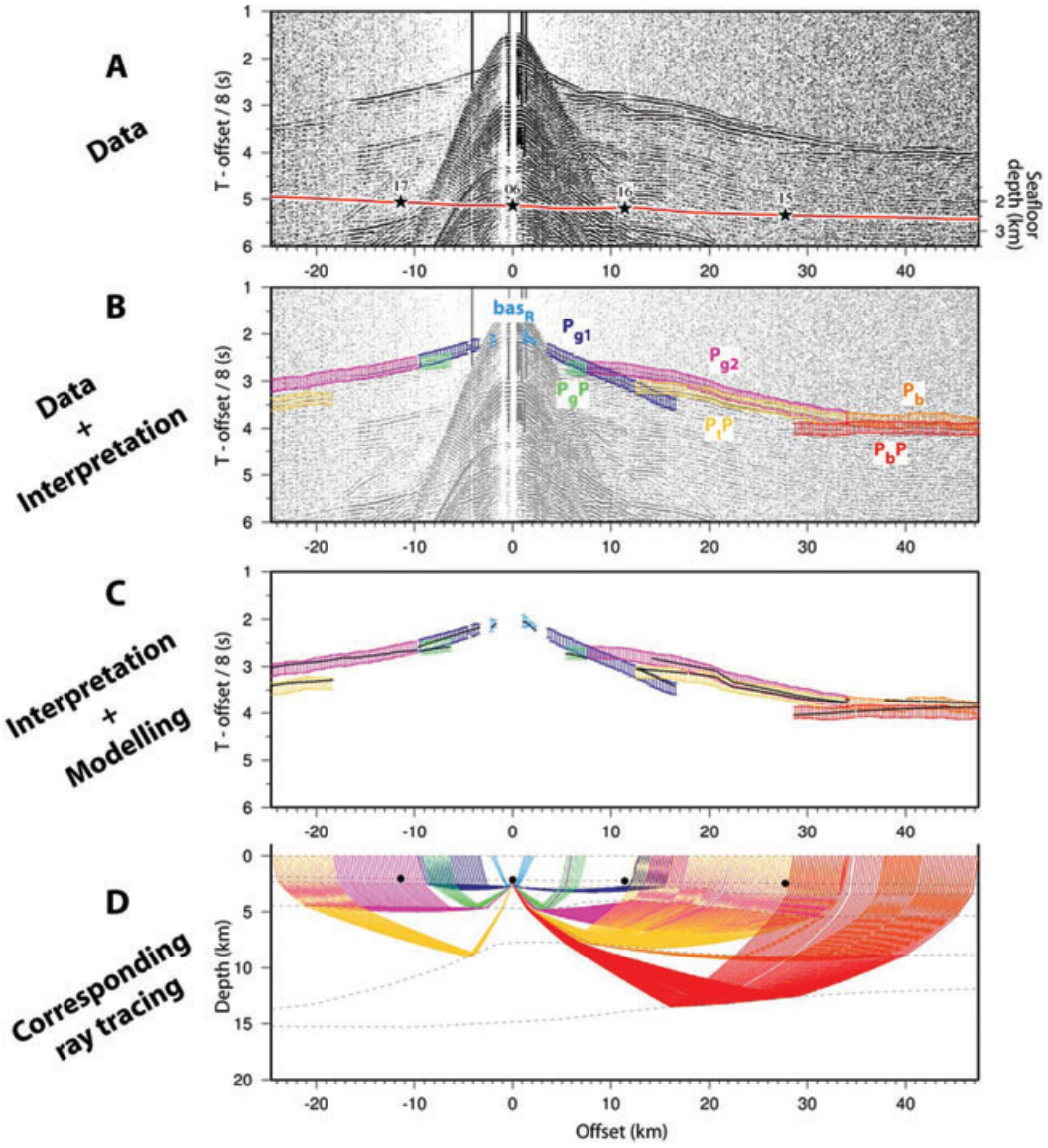

Figure 3. (A) OBS 06 record of shots along ENCR05 profile. A reduction velocity of 8.0 km s^{-1} is applied. Red line corresponds to the bathymetry and black stars are OBS positions along the profile. Note the high amplitude wide-angle reflections. (B) Picks with variable uncertainties over the seismic record; colour code refers to interpreted phases (see Table 1). (C) Synthetic traveltimes from wide-angle modelling (black dots) superimposed to the picked traveltimes (same colour code as in B). (D) Corresponding ray tracing (same colour code as in B).

Table 1. Glossary of seismic phases.

Phase	Description
WW	Direct wave through the water
sed_{2R}	Intra-sediments reflection
sed_2	Refraction in the second sedimentary layer
bas_R	Reflection at the basement top
P_{g1}	Refraction in the upper-crust
P_gP	Intra-crustal reflection
P_{g2}	Refraction in the lower crust
P_mP / P_tP	Reflection on the Moho/ at the top of an intermediate velocity body at the base of the crust
P_b	Refraction in the intermediate velocity body
P_bP	Reflection at the base of the intermediate velocity body
P_n	Refraction in the upper-mantle

Table 2. Modelling statistics for each wide-angle seismic lines (*N*, number of observations to which rays were successfully traced, and RMS is the root mean square misfit between picked and synthetic traveltimes.)

Line	*N*	RMS (s)	χ^2
ENCR01	1978	0.137	1.703
ENCR02	4964	0.123	1.358
ENCR04	2493	0.063	2.509
ENCR05	2638	0.045	0.876
ENCR07	2796	0.102	1.195
ENCR09	4173	0.123	3.504

reflection in the MCS, the passage from syn-rift to syn-OCT/post-rift sediments (U1 and U2-5, Figs 6 and 7).

The bottom of these syn-to-post rift sediments is the top of the acoustic basement imaged by MCS lines (Autin *et al.* 2010). Top

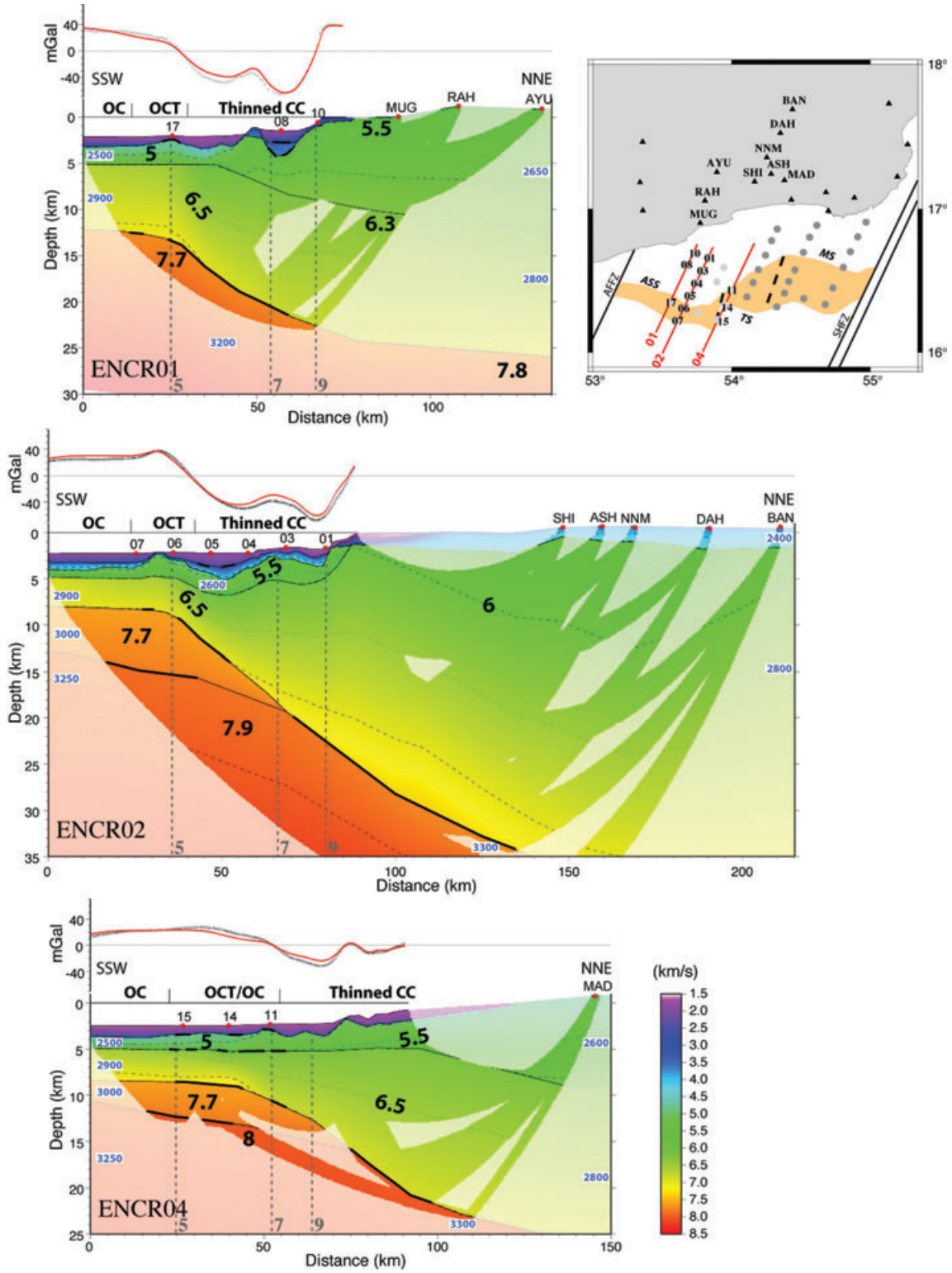

Figure 4. *P*-wave velocity models of across strike lines of the margin (ENCR01, ENCR02 and ENCR04 profiles). The mini-map shows the location of these 3 shots-lines. The upper panel is free-air gravity measured (black crosses) and modelled (red lines). In the lower panel, velocities are showed using a colour scale. The colours are saturated in areas effectively crossed by seismic rays. Purple to blue colours are typical velocities for sediments, green to yellow layers are likely the crust (continental as well as oceanic). Orange layer (ENCR02, and 04) velocities are neither typical crustal velocities nor upper-mantle velocities), and orange to red colours are typical of the upper-mantle. Thin continuous black lines are model interfaces. Thick black segments are the portions of interface effectively hit by wide-angle reflections. Dashed lines are isovelocity lines every 1 km s^{-1}, up to 6 km s^{-1}, and every 0.5 km s^{-1} above. Black numbers within layers are representative velocity values. Blue values on white labels are layers densities (in kg m^{-3}). Gravity modelling provide extra constrains on the structures of the velocity models where there is no WAS coverage. OBS and landstations are shown by red circles at the surface. The instruments (OBS and landstations) are labelled only if used in the WAS modelling. Vertical grey dashed lines indicates intersections with other profiles. All models are presented at the same scale (vertical exaggeration: 2.67).

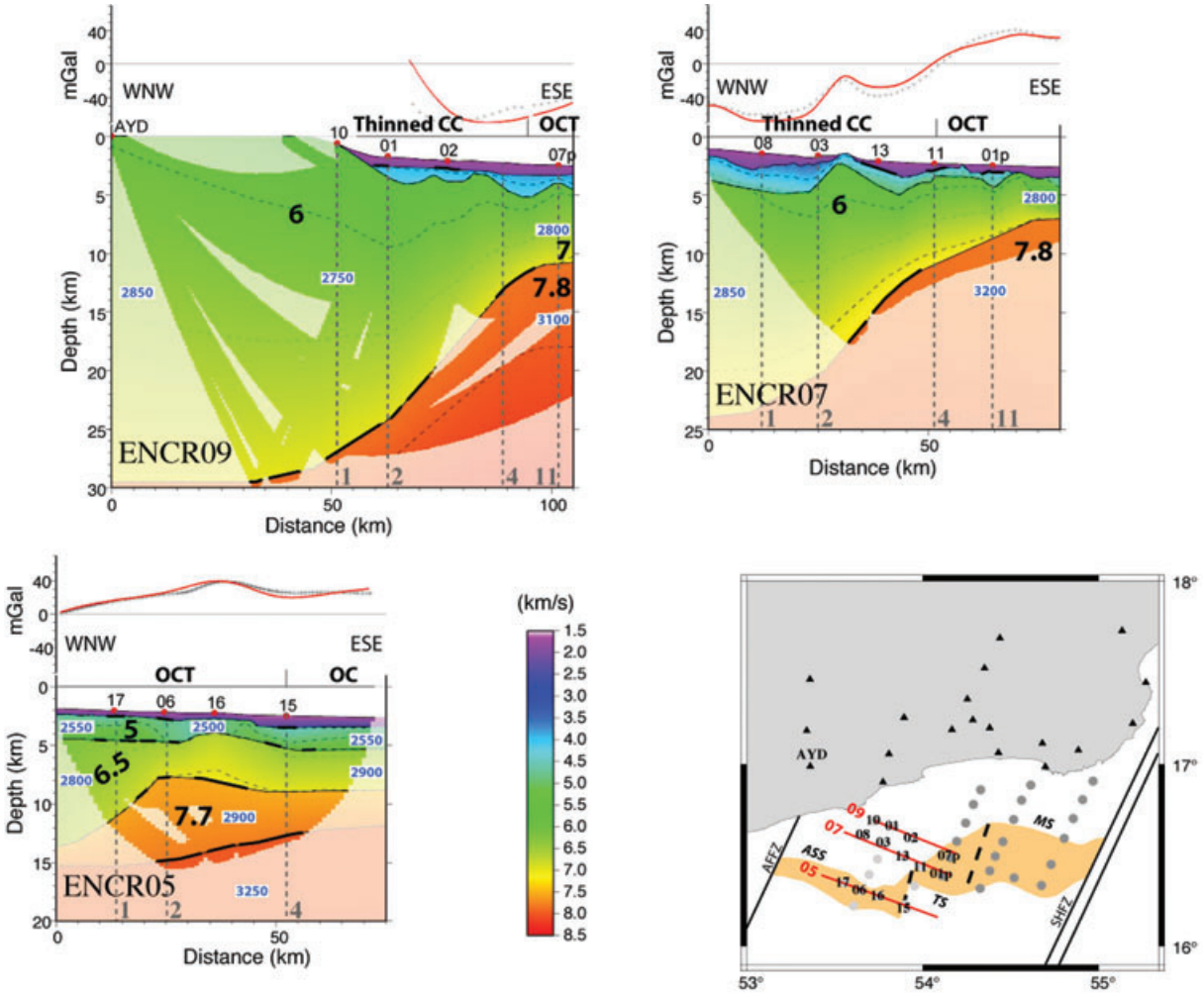

Figure 5. *P*-wave velocity models for along strike lines (ENCR05, ENCR07 and ENCR09 profiles). Same comments as in the caption of Fig. 4.

of the acoustic basement imaged here corresponds to pre-rift/syn-rift interface in continental domain and L1/L2 interface in oceanic domain.

4.1.2 Upper and lower acoustic basements

The top of the acoustic basement corresponds to a major velocity jump seen on all WAS records (from 4.2 to 5.5 km s^{-1} in the continental domain and from 2.2–4 to 4.5 km s^{-1} in the oceanic domain). The velocity below is significantly higher than the faster sediments. In the WAS, the middle crust interface shape the acoustic basement top. In the MCS, several structural highs shape the top of the crust, both in the continental slope and in the transitional domain (Fig. 6). The highs have a strong signature in the shape of all the refracted P_{g1} and P_{g2} phases (Fig. 8). The velocity of the volcano edifice (5.5 km s^{-1}, Fig. 4) is slightly higher than the surrounding (5 km s^{-1}). Note that velocities observed in the volcano are compatible with common volcanic structures (e.g. Klingelhoefer *et al.* 2001; Lizarralde *et al.* 2002).

The transition between continental and oceanic crusts appears gradually on the velocity models. The oceanward limit of the OCT is not a bias from the OBS positions. Indeed, it is determined by the identification of the A5d magnetic anomaly which is totally independent. More OBS were planned to be deployed oceanward, but some technical issues did not allow these deployments. Thus we chose to keep a lot of OBS on the margin to have a better resolution there. However, the structure of the oceanic crust is imaged with some rays traced in the oceanic domain (over 10 to 40 km distance for all models showing oceanic crust, see bright areas on Figs 4 and 5, profiles ENCR01, 02, 04 and 05) and gravity modelling. Along the continental slope, the velocity below the top of basement interface is commonly 5 to 5.5 km s^{-1} whereas it is not higher than 4.5 km s^{-1} oceanward (Figs 4 and 5). This variation is correlated with the contrasted nature of the crust in the oceanic and continental domains (respectively assumed as oceanic layer 2; L2; and pre-rift sediments). Indeed, oceanic layer 2 is known to have *P*-wave velocities ranging from 3.25 to 6.25 km s^{-1} for a context of slow spreading ridge (Atlantic Carlson & Raskin 1984) whereas limestones can show velocities up to 6.1 km s^{-1}, depending on the compaction (Gaviglio 1989). Pre-rift sediments in the Gulf of Aden are known to be mostly Cretaceous to Lower Tertiary limestone (e.g. Roger *et al.* 1989; Brannan *et al.* 1997). Thus, the pre-rift sediments are probably strongly compacted, showing a high *P*-wave velocity (5.5 km s^{-1}) which can be higher than the oceanic L2 velocity. Locally in the transition zone, the upper-crust velocity can be even lower (*cf.* ENCR01 at 34 km, Fig. 4). Reflected as well as refracted events differentiate a lower crust oceanward, in which

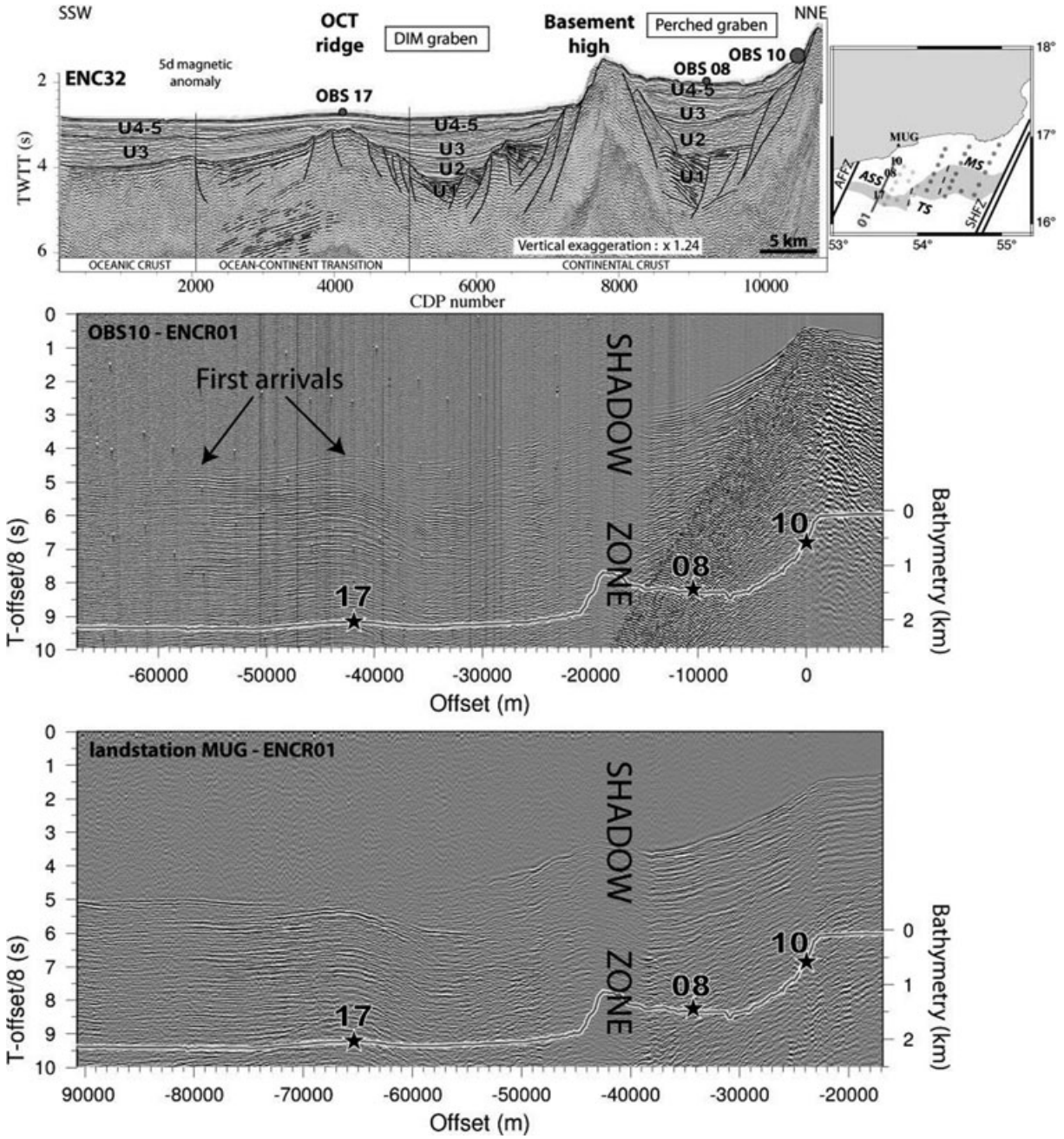

Figure 6. Comparison of MCS and wide-angle data along the coincident profile. Upper panel: ENC32 MCS profile and its interpretations. U1 are syn-rift sediments unit, U2 are syn-oct sediments unit and U3 and U4-5 are post rift-sediments units defined by Autin *et al.* (2010). Lower panels: wide-angle seismic coincident line ENCR01 recorded by OBS 10 (top) and landstation MUG (bottom). The map on the right-hand side shows the location of the profile, as well as the two stations for which records are shown below (orange area is the extent of the OCT, *cf.* Fig. 2).

the velocity is higher than 6 km s^{-1} (ENCR01, 02, 04 and 05). The velocity in the lower crust shows a bimodal distribution: the velocities are significantly higher in the oceanic and transitional domains (>6.5 km s^{-1}) whereas the lower continental crust is characterized by lower velocities (∼6 km s^{-1}). This oceanward velocity increase in the deep crust appears to be relatively sharp for ENCR01 and 02 (over less than 20 km) and more progressive along ENCR04 (Fig. 4).

The depth of the interface between the upper and lower crusts is approximately 5 km in the OCT and oceanic domains; it is well constrained by wide-angle reflections on ENCR04 and 05 (Figs 4 and 5). Continentward, these reflections and refractions vanish. The wide-angle seismic data do not support any velocity jump, differentiating a faster lower unit. Accordingly, the velocity is set continuous across this interface. This ghost interface is used to ascribe a stronger velocity gradient in the upper continental crust where fast events are observed at near-offset (Fig. 4, ENCR02 velocity model, below the continental slope). Wide-angle reflections constrain the thickness of the continental crust to 35 km (Fig. 4, ENCR02).

The oceanic crust (oceanward the A5d magnetic anomaly) is characterized by the typical velocity structures of layers 2 and 3 (White *et al.* 1992). Vertical gradient of upper oceanic crust is

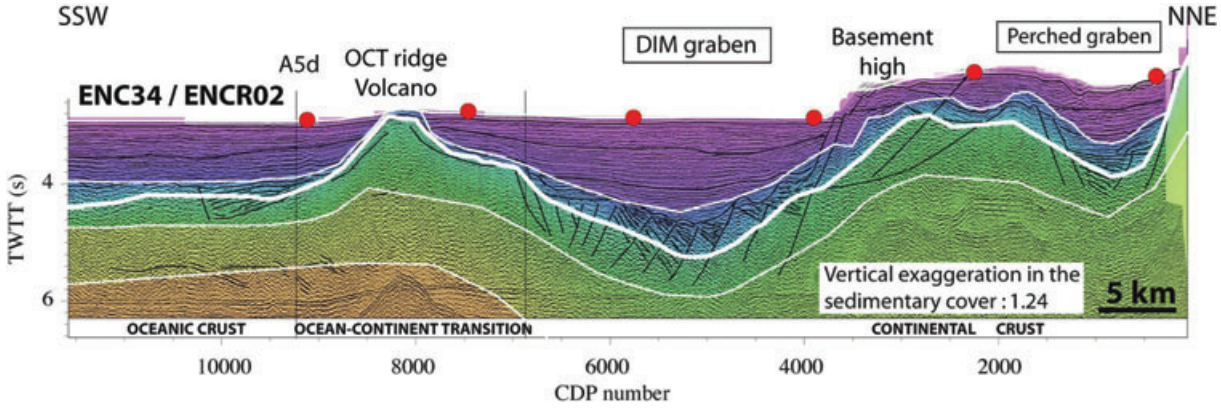

Figure 7. Comparison of ENC34 depth-migrated MCS (Autin *et al.* 2010) and wide-angle on the coincident ENCR02 profile. Blacks lines are line drawings of the seismic line ENC34 and white lines are ENCR02 model interfaces. The thickest white interface is the WAS top of basement. Colour scale is the same as in Fig. 4.

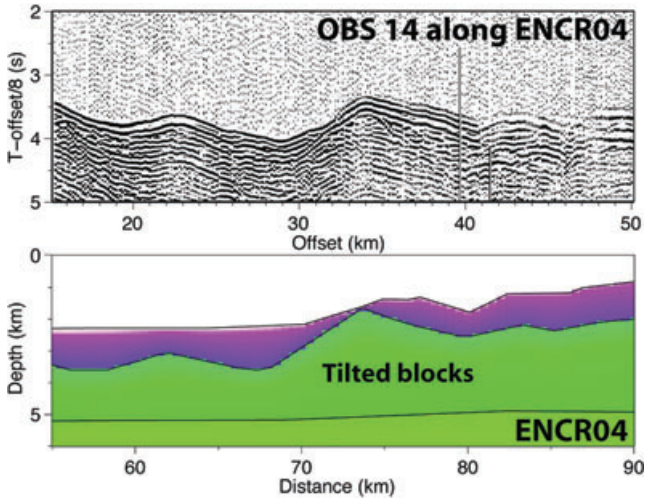

Figure 8. Upper panel shows a detail of the OBS 14 seismic record (reduction velocity of 8 km s^{-1}) along ENCR04 shot line and lower panel shows a detail of the coincident velocity model. Note the expression of the basement relief on the apparent velocities on the seismic section. Colour scale is the same as Fig. 4.

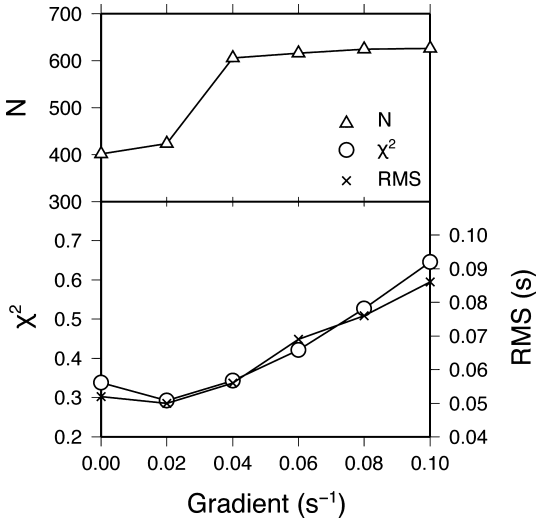

Figure 9. Analysis of modelling statistics (N, χ^2 and RMS) for ray tracing for the phases P_b and P_bP, i.e. in the intermediate velocity/density body, as a function of the velocity gradient in this structure. Note that the number of rays traced is higher for a velocity gradient of 0.04 s^{-1}, with low values of χ^2 and RMS.

about 0.5 to 1 s^{-1} while lower oceanic crust one is only 0.1 to 0.2 s^{-1}, which is typical from oceanic layers 2 and 3 (0.65 s^{-1} for L2 and 0.18 s^{-1} for L3; White *et al.* 1992). The oceanic lower crust thickness is thinner along ENCR02 and 04 (3 to 3.5 km, half the thickness of ENCR01 oceanic lower crust).

4.1.3 Lower crustal intermediate velocity body

A striking feature of the deep velocity structure along ENCR02, 04 and 05 is the presence of a double reflector encapsulating a 7.6–7.8 km s^{-1} body below the transitional domain. Fig. 3 is the record of ENCR05 by OBS 06, showing the reflected and refracted phases constraining this intermediate velocity body. The choice of the vertical velocity gradient in this structure is led by an analysis of the statistics for models testing this parameter (Fig. 9). The velocity in the upper part of this structure is set by the interpretations of the P_b refracted phase. The shape of the interface at the base of this body is determined by the interpretation of the P_bP wide-angle reflections and the testing of the velocities at its base. This double reflector and the seismic rays constraining it are shown in greater details in Figs 10 and 11 and data are shown in Fig. 12. This body reaches a thickness of more than 5 km below the volcano. It is important to note that the thicker oceanic crust found along ENCR01 is compatible with the presence of this intermediate body: no internal reflection is observed along this line, but the line is unfortunately not long enough oceanward to provide the proper offsets. The thickening of the crust and the intermediate body are indeed observed below OBS 17 on ENCR05, at the intersection with ENCR01 (Figs 4 and 5). This suggests the presence of the intermediate body below the OCT and oceanic domains on the ENCR01 profile.

4.1.4 Moho and upper mantle

Numerous P_mP phases constrain the base of the crust interface below the continental slope and the transitional domain (thick black segments of interfaces on Figs 4 and 5). The layer below is characterized by velocities close to 8 km s^{-1}, suggesting that the mantle

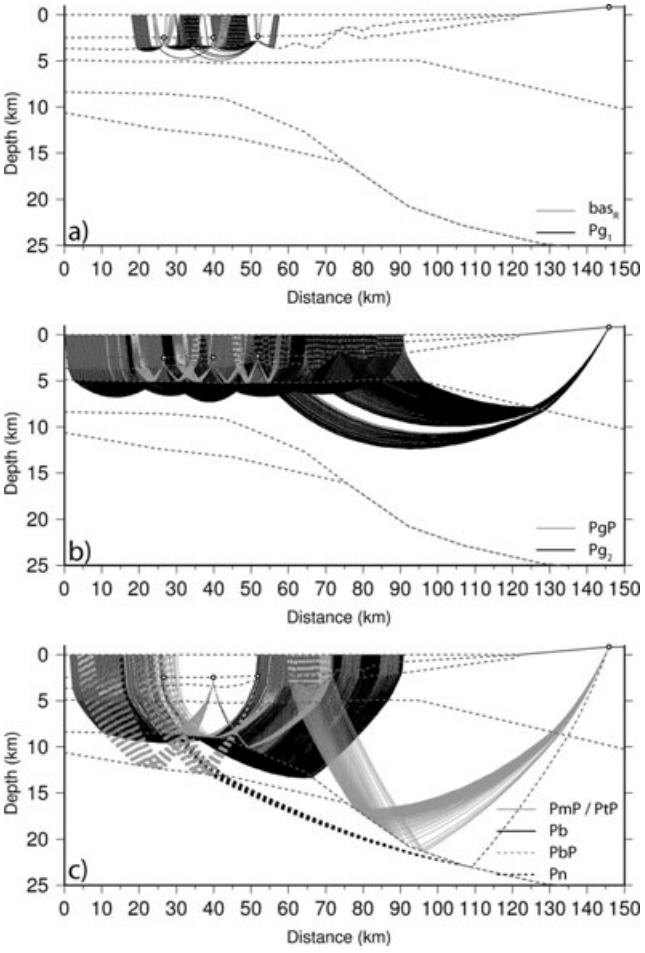

Figure 10. (a) Ray coverage of the upper crust along ENCR04 (every second ray). (b) Same as (a) but for the lower crust. (c) Same as (a) but for the high-velocity lower crust or low-velocity upper mantle body and upper mantle layer.

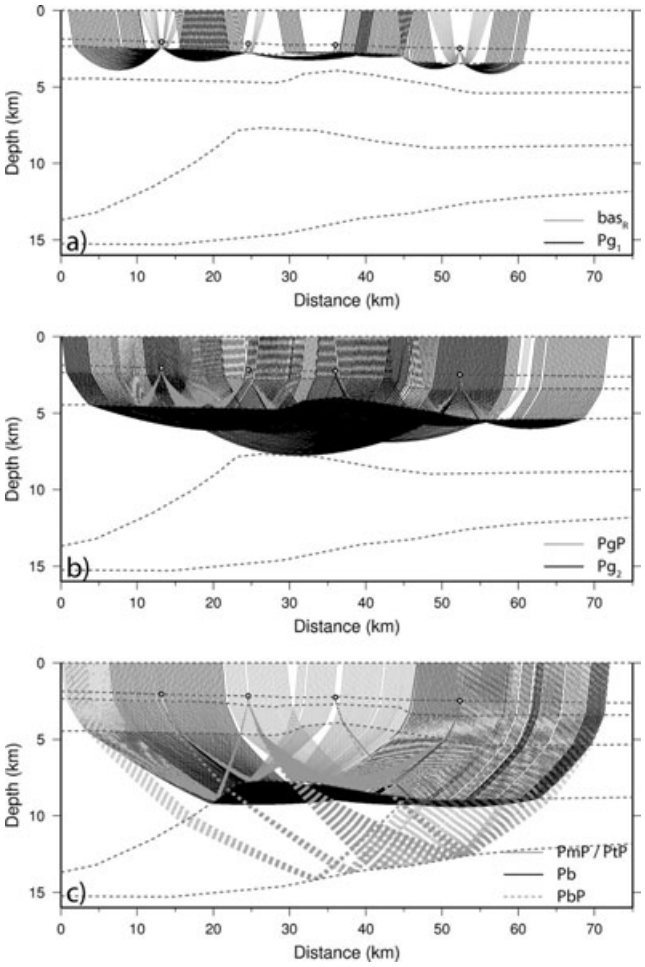

Figure 11. Same as Fig. 10 but for ENCR05.

is reached. On profiles ENCR01, 02, 07 and 09, mantle velocities are uniformly low, with values ranging from 7.8 to 7.9 km s^{-1}. The relatively low values for the expected mantle are constrained by P_n phases expending on a wide range of offsets and along independent directions.

4.2 Models resolution

The χ^2 and RMS parameters provide a first quantitative information on the ability of the velocity model to account for the interpretation of the traveltimes (Tables 2 and A1). Further, the fits between picked and synthetic traveltimes give a qualitative information (Fig. A1).

Ray coverage highlights areas densely crossed by seismic rays and unconstrained areas (Figs 10 and 11). One checks that the features of the velocity models are supported by numerous rays of different OBS, with different offsets, providing the appropriate redundancy. Further, the quality of the velocity model can be estimated using the resolution parameter (Zelt & Smith 1992). Fig. 13 shows the diagonal value of the resolution matrix for all velocity nodes. It is an estimate of the number of rays constraining the considered velocity node; it is therefore dependant on node density. The resolution varies from 0 to 1; a value higher than 0.5 is considered as a good resolution. As post-rift sediments were picked on coincident MCS for all profiles except ENCR07, resolution for this layer is arbitrarily set to 1. Crustal layers are generally well resolved, as well as the intermediate body (Fig. 13). With a total of 1592 rays refracted in the intermediate body and 590 rays reflected at its base, this structure is well constrained.

A low resolution is observed in the basement high along ENCR01 (in Fig. 4 abscissa 54 km and over the basement high observed in MCS data, Fig. 6). This basement high corresponds to a shadow zone in the WAS data, possibly resulting from a highly tectonised unit (Fig. 6) where seismic energy is diffracted. This shadow zone is only observed on this high of basement on ENCR01 and not obvious on the eastward continuation of the high (ENCR02 and 04). This may be due to the fact that the high of basement is covered by sediments on ENCR02 and 04 and not in the profile ENCR01. Seismic energy may be diffracted where the impedance contrast is too high.

The resolution in the crust along profiles ENCR07 and 09 is good thanks to the limited number of velocity nodes involved (more velocity nodes do not improve significantly the data fit). Furthermore, the velocity in the continental crust is apparently well resolved but only constrained by shots in one direction, as there were no shots fired on land.

The fit of the velocities and depth of interfaces at the intersection of cross-cutting profiles is almost always good. The misfit between interfaces is usually lower than 1 km.

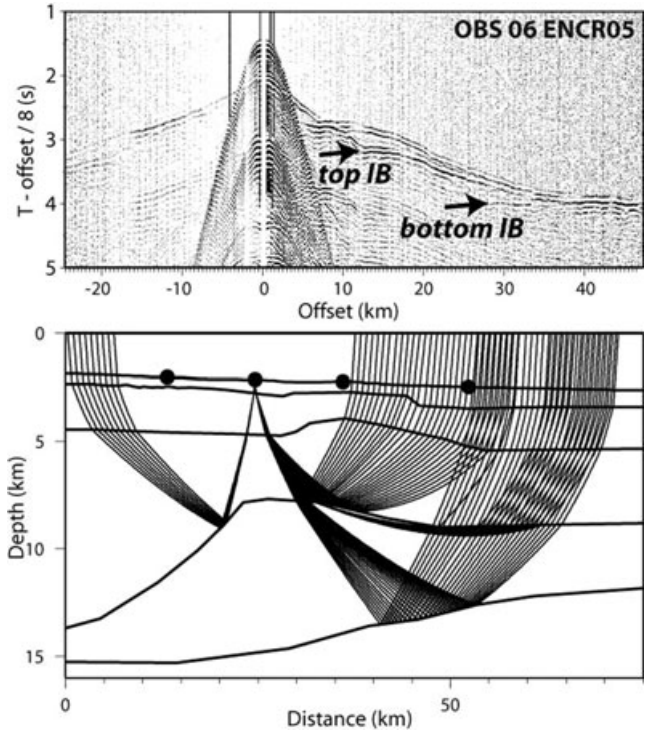

Figure 12. Upper panel: OBS 06 record section on ENCR05 shot line. IB: intermediate velocity body reflections. Lower panel: Ray tracing diagram for top of the intermediate body reflections, refractions in the intermediate body and reflections on the base of the intermediate body.

4.3 Density distribution

With a misfit generally lower than 20 mGal, the observed and computed gravity anomalies are in reasonable agreement without any *ad-hoc* density adjustment in the crust. Local gravity highs closely match the basement highs, showing that the main source for the short wavelengths originates in the top of the basement topography (Figs 4 and 5), suggesting that the mere velocity–density conversion law of Ludwig *et al.* (1970) is appropriated in the crustal layers. Longer wavelengths mainly correlate to the crust/mantle interface structure. The densities have been hand-edited below the crust to improve the fit to the longer wavelengths. An overall value of 3100–3250 kg m^{-3} gives the best fit, with a density as low as 2900–3000 kg m^{-3} in the intermediate velocity body (Figs 4 and 5). Thus, both velocity and density in the mantle of the OCT area are found lower than the commonly observed values (respectively 8 km s^{-1} and 3300 kg m^{-3}). However, the modelling of gravity anomaly suggests that the mantle density tends to increase to 3300 kg m^{-3} continentward, beyond the seismic lines.

5 DISCUSSION

5.1 The intermediate velocity/density body at the crust–mantle interface

Structures with velocities ranging from 7.2 to 8 km s^{-1} are frequently observed below passive continental margins and are related to various geodynamical contexts. (1) On magma-poor rifted margins, this intermediate velocity layer can be more than 5 km thick and extend up to 200 km below the thinned continental crust and oceanic crust (Lau *et al.* 2006). Drilling demonstrated the partially serpentinised nature of continental and oceanic mantle, likely resulting from the fracturation and seawater percolation (e.g. Boillot *et al.* 1989; Cannat 1993; Beslier *et al.* 1996). Laboratory experiments show that 10 per cent serpentinised mantle may result in a *P*-wave velocity as slow as 7.5 km s^{-1} (Horen *et al.* 1996). The entire crust becoming brittle for stretching factors ranging between 3 and 5, seawater may penetrate into depth along the faults and serpentinise the upper-mantle (Pérez-Gussinyé & Reston 2001). (2) On the opposite, volcanic margins commonly feature an intermediate velocity body. They are usually interpreted as underplating of mafic rocks trapped at the base of the crust, but no direct evidence of igneous materials could confirm this statement so far (e.g. Geoffroy 2005).

Table 3 gathers some physical characteristics of intermediate velocity structures observed on various margins. It suggests that the vertical velocity gradient may be relevant to discriminate between serpentinised upper-mantle versus mafic body. Gradients higher than 0.08 s^{-1} are typical serpentinite, while gradients lower than 0.05 s^{-1} may characterize mafic body. Moreover, mafic bodies correlate with greatest thicknesses. According to the few examples shown in Table 3, 5 to 6 km could be the threshold value. The intermediate velocity body observed in the study area shows a maximum thickness of 5 km for velocities ranging from 7.6 to 7.8 km s^{-1}; it leads to a vertical velocity gradient of 0.04 s^{-1}, which supports the mafic body hypothesis.

Furthermore, Minshull (2009) compiles the WAS studies on margins, pointing out the differences in terms of seismic velocity: the serpentinised mantle thickness is restricted to *ca*. 6 km by thermal conditions, whereas the underplated bodies can be thicker. The seismic crust above the serpentinised mantle is slow and thin, while the crust above the underplating is generally thick and faster than the continental crust. Eventually, the underplated body is expected to exhibit a double reflector in the wide-angle records, related to the velocity jumps at the top and bottom of the mafic body (abrupt changes in the mineralogy). Minshull *et al.* (2008) also suggests that the double reflector should not be observed at partially serpentinised mantle margin because the velocity contrast at the crust–mantle interface is attenuated and the serpentinisation rate is expected to decrease progressively downward, providing no abrupt change in the physical properties. However, a double reflector has been observed in some supposed serpentinised upper-mantle (Table 3, Reid 1994; Chian *et al.* 1995; Funck *et al.* 2004). Velocity models along these profiles show a velocity jump at the base of these bodies, implying abrupt changes in mineralogies. This may result from the sealing of faults, due to the increase of volume associated to the serpentinisation process (e.g. Schroeder *et al.* 2002).

In our study, a double reflector is clearly identified along several profiles, encapsulating the intermediate velocity body, featuring a low velocity gradient and a thickness of approximately 5 km. The double reflector together with the low velocity gradient, promotes the mafic body interpretation.

Three ways to produce igneous material at the base of the crust are possible: (1) high initial asthenospheric temperatures cause intrusions in the lower crust and volcanic activity at the surface during the thinning of the lithosphere (e.g. White *et al.* 1987; Morgan *et al.* 1989; Barton & White 1997; Funck *et al.* 2008), (2) magma pounding due to adiabatic decompression of asthenosphere beneath the stretched lithosphere, the material rises to the surface at the time of the final continental rupture (e.g. Keen 1987; Morgan *et al.* 1989), or (3) small scale convection cells induced by high temperature gradient and enhanced by the break-up process, adding igneous material to the oceanic crust (e.g. Mutter *et al.* 1988; Morgan *et al.* 1989; Holbrook *et al.* 1994a,b; Bauer *et al.* 2000).

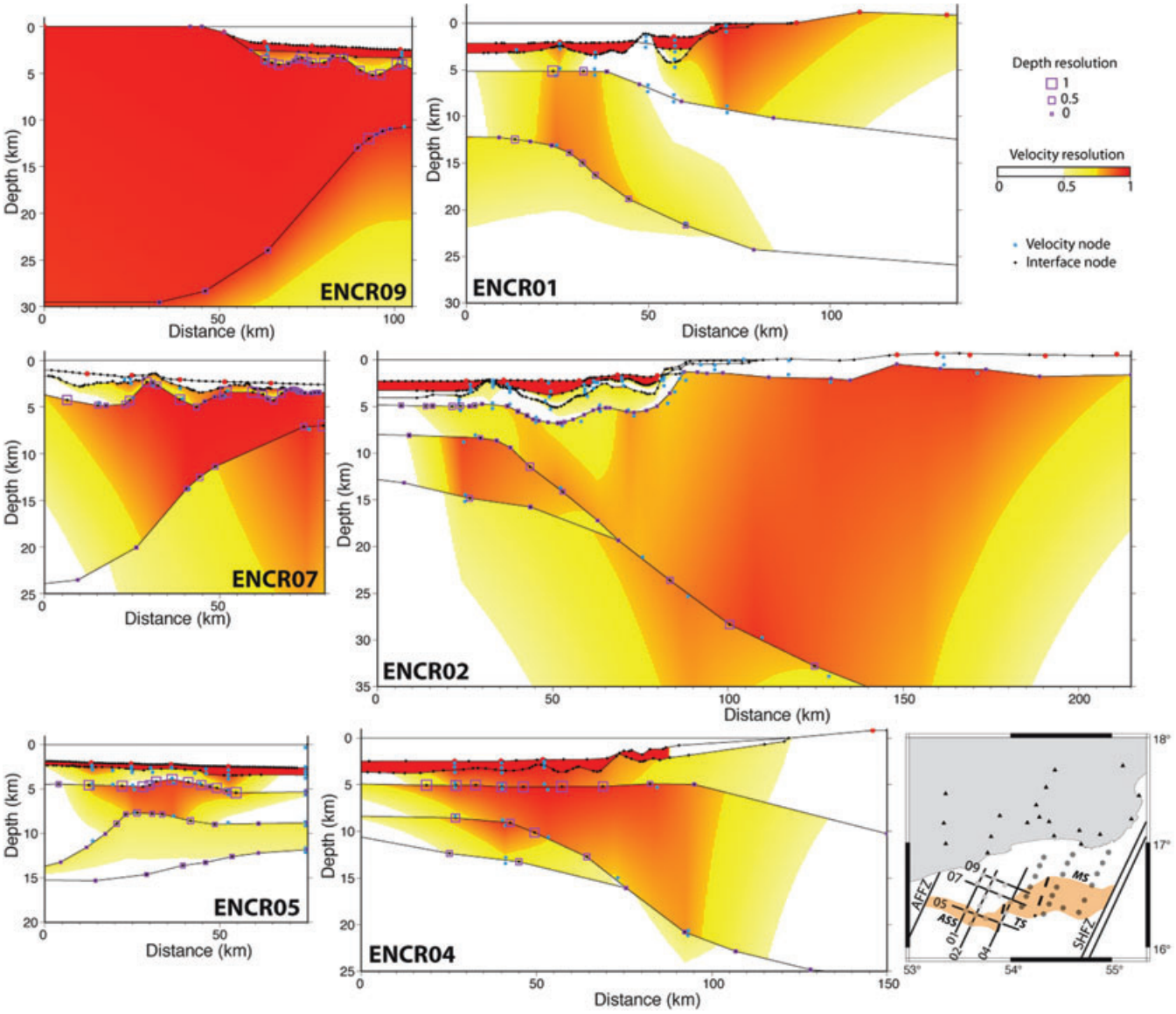

Figure 13. Resolution diagrams for the six velocity models. Resolution of velocity nodes is shown by the white to red colour-scale. Orange to red gradation areas are considered very well resolved (resolution between 0.75 and 1) and yellow areas (resolution between 0.5 and 0.75), well resolved. Resolution of the depth for each interface nodes is shown by the purple squares. The larger is the square, the better is the resolution. Velocity and interface nodes are highlighted by blue circles and black dots, respectively. Red circles correspond to OBS and land-seismometers positions.

The volcano at the intersection of ENCR02 and 05 is located above the thickest part of the intermediate velocity body. It is therefore sensible to relate the volcano to this structure. Autin *et al.* (2010) show that volcanism occur just after the emplacement of the OCT basement and the post-rift sediments. We show here wide-angle reflections both at the top and bottom of this structure beneath the OCT crust and the earliest oceanic domain. Thus, as in the Autin *et al.* (2010) paper, the extent of the intermediate body underneath the oceanic and transitional crusts suggests that its emplacement is late or goes on immediately after the onset of oceanic accretion.

A discussion often concerns whether the mafic body is trapped at the base of the crust for rheological or density reasons, or if it intrudes the lower crust as sills (Funck *et al.* 2008). The observations of the post-rift sediments recorded by the MCS (Autin *et al.* 2010, see Fig. 7 for location) shows a post-rift magmatic activity, with a post-rift growth of an OCT ridge. Thus, the volcanic structure is early post-rift to post-rift, as corroborated by Lucazeau *et al.* (2009) and Autin *et al.* (2010). Ashawq–Salalah segment is close to the major Alula–Fartak fracture zone that separates thick continental crust in the West from the distal margins of the Ashawq–Salalah segment. Gregg *et al.* (2007) suggest that fracture zones along ridges may increase thermal anomalies by small-scale convection. Moreover, observations on bathymetry, gravity and magnetism suggest the presence of melting anomaly located in this segment (d'Acremont *et al.* 2010) that shows typical characteristics of plume-ridge interaction (Leroy *et al.* 2010a). In summary, the intermediate body may be interpreted as underplated body coming from a small-scale convection processes due to edge effect of the continental margin on Alula–Fartak fracture zone, or from channelling plume-ridge interaction (Leroy *et al.* 2010a) as early as the beginning of seafloor spreading, or from both. The body maximum thickness is approximately 5 km, which is lower than the thicknesses of typical syn-rift underplated bodies observed along volcanic margins (Table 3). Furthermore, this underplated magma may partly intrude the lower

Table 3. Comparison of intermediate velocity/density bodies characteristics and natures from various margins. Rows are sorted by decreasing gradients. $Th.$ is for the the maximum intermediate body thickness, $Grad.$ is the the vertical velocity gradient of the structure, S.U.M. is for serpentinised upper-mantle and *M.B.* is for mafic body. Note that higher velocity gradients are for serpentinised mantle. [a]indicates that wide-angle reflections are observed at the base of the intermediate body.

References	Location	Line	V_P (km s^{-1})	$Th.$ (km)	$Grad.$ (s^{-1})	Interpretation
Van Avendonk *et al.* (2009)	Newfoundland	Screech-II	5.3–8.1	5	0.560	S.U.M.
Lau *et al.* (2006)	Newfoundland	Screech-III	6.4–7.8	3	0.460	S.U.M.
Chian *et al.* (1995)	Labrador	90R1	6.4–7.7	5	0.260	S.U.M.[a]
Dean *et al.* (2000)	S.I.A.P.	IAM-9	7.3–7.9	3.5	0.171	S.U.M.
Reid (1994)	Newfoundland	Line 7	7.2–7.6	4	0.100	S.U.M.[a]
Funck *et al.* (2003)	Flemish Cap	Screech-I	7.6–8.0	5	0.080	S.U.M.
Funck *et al.* (2004)	Nova Scotia	Line 1	7.2–7.6	5	0.080	S.U.M.[a]
Barton & White (1997)	Edoras Bank	Cam 77	7.2–7.6	8	0.050	M.B.
Bauer *et al.* (2000)	Namibia	Transect 1	7.6–7.8	7	0.029	M.B.[a]
Hirsch *et al.* (2009)	SW Africa	Springbok	7.0–7.4	16	0.025	M.B.[a]
Holbrook *et al.* (1994a)	Virginia	Line 801	7.1–7.5	18	0.022	M.B.[a]
Minshull *et al.* (2008)	Arabian Basin	Ø	7.4–7.6	11	0.018	M.B.[a]
Funck *et al.* (2008)	Faroe Islands	Line A	7.3–7.4	6	0.017	M.B.[a]
Morgan *et al.* (1989)	Hatton Bank	Ø	7.3–7.4	14	0.007	M.B.

crust during the post-rift as for the syn-rift volcanism observed on volcanic margin (e.g. Geoffroy 2005).

5.2 Thinning of the continental crust

Thinning of the continental crust from 35 to approximately 8 km is accommodated by three or four tilted blocks bounded by normal faults, featuring syn-rift, fan-like deposits within the continental slope (d'Acremont *et al.* 2005). These tilted blocks are imaged on MCS sections (Autin *et al.* 2010; Leroy *et al.* 2010b), WAS and gravity data offshore (Figs 7 and 8) and observed onshore (Fig. 2).

Most of the thinning occurs over 50 to 100 km (ENCR01 and ENCR02, respectively, Fig. 14). A margin is defined as *hard* when the thinning occurs on less than 150 km (Davison 1997; Reston 2009). As the conjugate margin is twice larger and asymmetric (Leroy *et al.* 2004; d'Acremont *et al.* 2005, 2006), we may propose that the conjugate is *soft*, implying an asymmetry in the deep structure, and thus (1) an asymmetric rifting process leading to mantle exhumation (simple shear, Wernicke 1985; Boillot & Froitzheim 2001), or (2) a migration of the rifting location due to slow rifting (Kusznir & Park 1987; Bassi 1995). Table 4 shows the thinning values for some volcanic and non-volcanic passive margins. The higher thinning values for non-volcanic passive margins may be explained by the fact that (1) rifting processes are hotter along volcanic margins, implying that less thinning is needed to break the continental lithosphere (Hopper & Buck 1996; Buck 2004) and (2) some igneous material is brought to the base of the crust, leading to a thickening of the crust and a lower apparent thinning value.

For this study, the β factors are calculated from the Tiberi *et al.* (2007) maximum on land crustal thickness value (36.6 km) and the crustal thicknesses calculated from WAS. Crustal thicknesses are the differences between the top of the acoustic basement and the base of the crust, intermediate body excluded (as it is a post-rift structure, added after the thinning process). The maximum thinning factors (at the OCT boundary) are 3.2 for ENCR01 (minimum value as the intermediate body is not defined on this profile), 5.3 for ENCR02 and 4.8 for ENCR04. These later values are maximum values, as the intermediate body may partly intrude the lower crust. Crustal thinning is thereby particularly abrupt which is characteristic of magma-poor margins (Table 4). Thinning values along this margin range from 3.2 to 5.3, allowing the crust to become totally brittle and thus serpentinisation to reach the upper-mantle (Pérez-Gussinyé & Reston 2001).

Thus, β factor values indicate a magma-poor margin context with potentially serpentinised upper-mantle. Autin *et al.* (2010) propose that the late volcanic activity may has erased the evidences of serpentinisation that could explain why we observe no evidence of serpentinised upper-mantle on the data: no S-reflector on the MCS, no high velocity gradient on WAS, and no serpentinisation-related magnetic anomaly (Leroy *et al.* 2010b).

5.3 Thickness of the oceanic crust

Fig. 15 shows representative vertical velocity profiles across the oceanic crust for ENCR01 to 05. Velocity values and gradients are typical of oceanic layers 2 and 3.

Along the 3 across margin profiles, the thickness of the oceanic crust, intermediate body excluded, varies from 10 km maximum in the West (centre of the Ashawq–Salalah segment, ENCR01) to less than 5.5 km on the East (in the Ashawq–Salalah segment and close to the Ashawq-Salalah/Taqah segment boundary, ENCR02 and 04) over a distance of ca. 10 km (ENCR05). The thickness variation affects both the lower crust and the upper crust, but most of the increase is accounted by the lower crust.

Previous WAS studies including data from worldwide normal oceanic crust (away from fracture zones or hotspot influences) show a mean thickness of 7.1 $\pm$ 0.8 km and extreme values of about 5.0 and 8.5 km for slow spreading rates (lower than 20 mm yr^{-1}, White *et al.* 1992; Bown & White 1994). The oceanic crust mean thickness is about 10.3 $\pm$ 1.7 km where upper mantle is hotter than normal and it can reach values higher than 20 km where the ridge interacts with a hotspot (White *et al.* 1992). The oceanic crust produced at volcanic passive margin is significantly thicker than 7 km (e.g. Morgan *et al.* 1989; Eldholm & Grue 1994; Barton & White 1997; Bauer *et al.* 2000). At smaller scale, the crust produced at the mid-oceanic ridges shows variable thickness. In the vicinity of ridge axis discontinuities, the oceanic crust is thinner, whereas the centre of segments usually shows the thickest crust (Rommevaux *et al.* 1994). Actually, the lower the spreading rate, the higher the variation of the crustal thickness (Salisbury & Christensen 1978; Bown & White 1994).

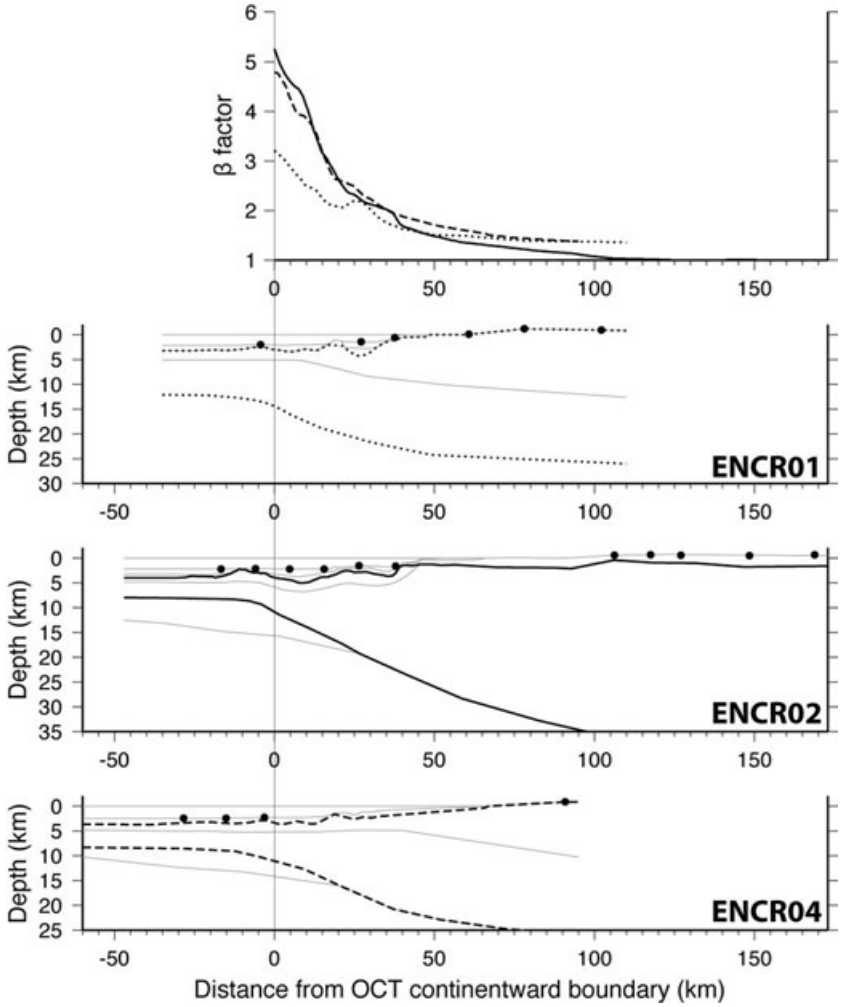

Figure 14. Top panel shows β factors calculated as the ratio max_{CC}/CTh with CTh the final crustal thickness and max_{CC} the maximum crustal thickness inferred by receiver functions (36.6 km, Tiberi *et al.* 2007). Curves are β factors excluding the intermediate velocity/density body of the crust thickness. The three lower panels are models interfaces. Bold interfaces are used for estimating crustal thickness. Dotted lines correspond to ENCR01, continuous lines to ENCR02 and dashed lines to ENCR04. This code is the same for the whole figure. The '0' distance value is constrained by the continentward OCT boundary (Autin *et al.* 2010; Leroy *et al.* 2010b).

Table 4. Comparison of β factors from various margins. Rows are sorted by decreasing β factors. *N.V.* and *V.* is for non-volcanic and volcanic margins, respectively. Note that higher β factors are for non-volcanic margins.

References	Location	Line	β factors	Margin type
Van Avendonk *et al.* (2009)	Newfoundland	Screech-II	10	N.V.
Funck *et al.* (2004)	Nova Scotia	Line 1	5.5	N.V.
Contrucci *et al.* (2004)	NW Morocco	Sismar profile 4	5	N.V.
Reid (1994)	Newfoundland	Line 7	5	N.V.
Bullock & Minshull (2005)	Goban Spur	WAM	4.5	N.V.
Lau *et al.* (2006)	Newfoundland	Screech-III	4.3	N.V.
Dean *et al.* (2000)	S.I.A.P.	IAM-9	4	N.V.
Klingelhoefer *et al.* (2009)	SW Morocco	Dakhla North profile	3.4	N.V.
Raum *et al.* (2002)	Vøring Basin	Transect1	2.9	V.
Bauer *et al.* (2000)	Namibia	Transect 1	2.6	V.
Morgan *et al.* (1989)	Hatton Bank	Ø	1.8	V.
Hirsch *et al.* (2009)	SW Africa	Springbok	1.8	V.
Hopper *et al.* (2003)	SE Greenland	Sigma-III	1.6	V.
Barton & White (1997)	Edoras Bank	Cam 77	1.6	V.

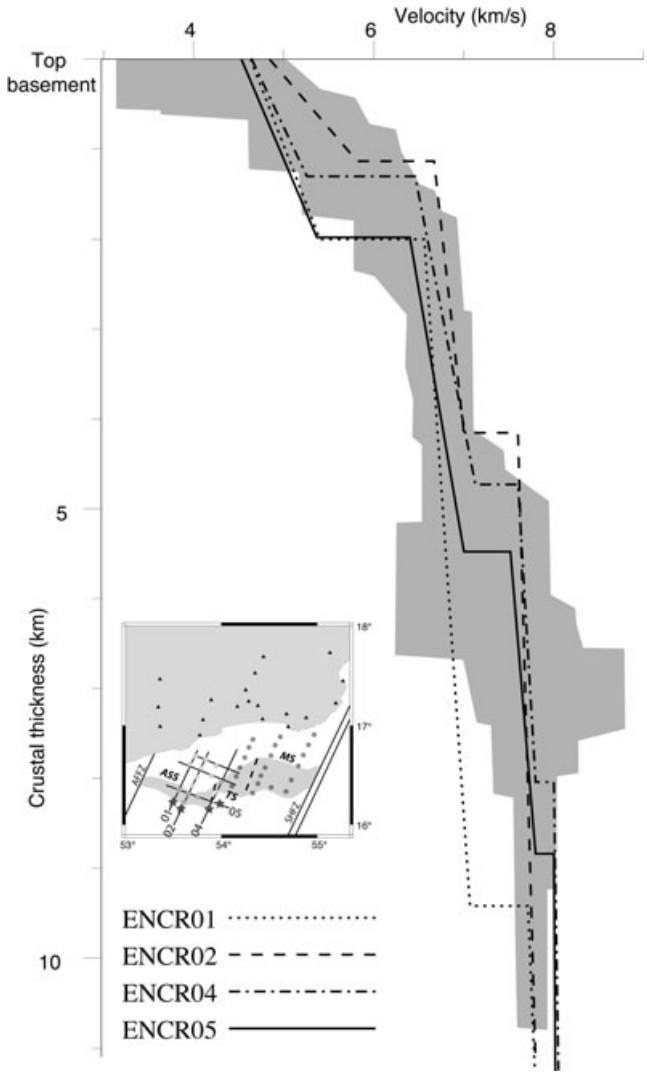

Figure 15. Velocity-depth profiles in the oceanic domain for ENCR01, 02, 04 and 05. As a comparison, the grey envelop marks the region enclosed by the highest and lowest values from the velocity-depth plots for a Pacific oceanic crust of about the same age (White *et al.* 1992, Fig. 5, Step 3–15 Ma). Velocity-depth profiles location is shown by red stars on the simplified trackmap.

The 10 km thick crust of ENCR01 could result from the formation of oceanic crust along a volcanic margin but a fraction of its thickness may be due to the presence of the thin underplated intermediate body. The decrease in the crustal thickness from west to east may be related (1) to the presence of a second-order discontinuity of the paleo-spreading axis in the vicinity of ENCR04 profile (Leroy *et al.* 2010b) and/or (2) to the melting anomaly observed apart from the present-day spreading axis, showing thicker-than-normal crust and off-axis volcanic activity in this ridge segment (d'Acremont *et al.* 2010). That could be related to plume-ridge interaction from the Afar plume along Aden-Sheba ridges system (Leroy *et al.* 2010a).

5.4 Nature of the transitional crust

Comparison of all profiles shows that both continental and oceanic domains are homogeneous along strike. These contrasted domains are separated by a transitional domain also identified though MCS, gravity and magnetism (Autin *et al.* 2010; Leroy *et al.* 2010b). The velocity models of the transitional domain feature (1) a blocky top-basement interface, similar to the one along the continental slope, and (2) a crustal velocity higher than in the continental domain. The velocities in the transition domain appear to be quite similar to the oceanic velocities and the two layers of the oceanic crust extend continentward until the continental crust is reached. The oceanward boundary of the OCT simply coincides with slick-to-rough transition of the top-basement, corresponding to the oldest seafloor spreading magnetic anomaly and to a 'flat' free-air gravity anomaly (Figs 4 and 5). However, the continental transition occurs through a strong horizontal velocity gradient, coincident with the abrupt deepening of the base of the crust. The velocity increase associated to the end of the thinning of the crust is a margin feature of all across strike profiles.

Thus, the OCT described in this study is a 15 km narrow stripe which compares better with the OCT width along volcanic margins (e.g. Barton & White 1997; Mjelde *et al.* 2007). However, the surface evidences of a high magmatic supply are subdued, compared to proven volcanic margins (oceanic crust thickness is lower than on volcanic margins and no SDR sequence is observed). Moreover, the continentward tip of the SDR wedge usually coincides with the further extent of the continental crust (Eldholm & Grue 1994; Planke *et al.* 1999; Bauer *et al.* 2000) whereas along ENCR02 profile the thin volcano-sedimentary edifice rather locates at the transition from the OCT and the oceanic domain (Fig. 7). As the thinning of the continental crust is large enough to cause mantle serpentinisation and as WAS data show no high velocity gradient in the OCT which may be a proof for upper-mantle serpentinisation, we propose that the OCT may be partly serpentinised mantle that was modified by later thermal event.

5.5 Low velocity/density upper-mantle

Low velocity/density upper-mantle is commonly observed on passive margins (*P*-wave velocities from 7.7 to 8 km s^{-1} and densities of 3200 kg m^{-3}; Pérez-Gussinyé *et al.* 2003; Fernàndez *et al.* 2004; Bullock & Minshull 2005; Lau *et al.* 2006). Mantle serpentinisation (Lau *et al.* 2006) or the presence of a thermal anomaly (Fernàndez *et al.* 2004) may explain these values. Lucazeau *et al.* (2008) showed that the eastern Gulf of Aden sustains a post-rift thermal anomaly persisting up to now: high heat-flow values are measured in adjoining segment of this margin by small-scale convection occurring during and after the rifting beneath the continental slope. The low velocity/density mantle observed here is in agreement with the presence of the post-rift thermal anomaly and consistent with the presence of the mafic body.

6 CONCLUSIONS

Modelling of the wide-angle data along the Ashawq–Salalah segment, north-eastern Gulf of Aden, constrain the crustal structure of the margin, from continental to oceanic domain.

Our main observations are:

(1) The thinning of the continental crust occurs over distances ranging from 50 to 100 km with thinning factors varying from 3.2 to 5.3. Such values suggest that the crust becomes entirely brittle during the end of the rifting with possible mantle serpentinisation according to Autin *et al.* (2010).

(2) The oceanic crust, intermediate body excluded, shows a drastic thickening along the margin possibly related to a variable magma supply along the slow spreading ridge and at the ridge centre, due to the paleo-ridge segmentation.

(3) A narrow OCT domain, approximately 15 km wide, exhibiting a post-rift volcanic activity, separates the thinned continental domain from the oceanic one.

(4) An intermediate velocity body at the base of the OCT and oceanic crusts, featuring a clear double reflector and a low vertical velocity gradient, interpreted as a post-rift mafic body probably related to the volcanic activity of the Ashawq–Salalah segment.

Thus, this margin shows some characteristic features observed on volcanic margins (volcano, mafic body) but these features seems to be post-rift events. Indeed, the volcano is located in the OCT, the mafic body double reflections are observed below the oceanic crust and its thickness is really lower than mafic body thicknesses observed at volcanic margins. So, the emplacement of this body is probably a post-rift event on a margin affected by few post-rift magmatism.

We conclude that this non-volcanic passive margin, characterised by a post-rift mafic body at the base of the crust and a volcano, is affected by a post-rift thermal anomaly. This thermal anomaly may have erased the WAS observation of serpentinisation that could be observed on non-volcanic passive margins.

ACKNOWLEDGMENTS

This project was funded by the GDRMarges; 'Actions Marges' and ANR YOCMAL projects. The data were acquired thanks to GDRMarges, INSU and Total funds. We deeply thank the officers and crew of R/V L'Atalante (Ifremer/Genavir) and the Géosciences-Azur 'OBS-Team': Yann Hello, Olivier Desprez and Alain Anglade for their implication in the wide-angle seismic data acquisition. We would like to thank Royal Holloway University of London, NERC/SEIS-UK and Sultan Qaboos University (Sultanate of Oman) who lent the landstations for the Encens cruise. We are grateful for Dr Hilal Al-Azri, Dr Salim Al Busaidi and Sami Zubedi for logistical support in Oman. Seismic-Unix (Stockwell 1997) and OBSTOOL (Christeson 1995) were used to process the wide-angle seismic data. The GMT software package (Wessel & Smith 1995) was used to produce the figures of this paper. We give a lot of thanks to Marie-Odile Beslier who spent some time to do comments which have contributed to improve this study. We thank Karsten Gohl, Philippe Charvis and Ingo Grevenmeyer for constructive reviews and comments.

REFERENCES

Autin, J., Leroy, S., d'Acremont, E., Beslier, M.-O., Ribodetti, A., Bellahsen, N., Razin, P. & Robin, C., 2010. Continental break-up history of a deep magma-poor margin from seismic reflection data (northeastern Gulf of Aden margin, offshore Oman), *Geophys. J. Int.,* **180,** 501–519.

Avedik, F., Renard, V., Allenou, J. & Morvan, B., 1993. Single bubble air-gun array for deep exploration, *Geophysics,* **58,** 366–382.

Barton, A. & White, R., 1997. Crustal structure of Edoras Bank continental margin and mantle thermal anomalies beneath the North Atlantic, *J. geophys. Res.,* **102**(B2), 3109–3129.

Bassi, G., 1995. Relative importance of strain rate and rheology for the mode of continental extension, *Geophys. J. Int.,* **122**(1), 195–210.

Basuyau, C., Tiberi, C., Leroy, S., Stuart, G., Al-Lazki, A.I., Al-Toubi, K. & Ebinger, C., 2010. Evidence of partial melting beneath a continental margin: case of Dhofar, in the Northern Gulf of Aden (Sultanate of Oman)., *Geophys. J. Int,* **180,** 520–534.

Bauer, K. *et al.*, 2000. Deep structure of the Namibia continental margin as derived from integrated geophysical studies, *J. geophys. Res.,* **105**(B 11), 25 829–25 853.

Bellahsen, N., Fournier, M., d'Acremont, E., Leroy, S. & Daniel, J.-M., 2006. Fault reactivation and rift localization: the northeastern Gulf of Aden margin., *Tectonics,* **25,** TC1007, doi:10.1029/2004TC001626.

Beslier, M., Cornen, G. & Girardeau, J., 1996. Tectono-metamorphic evolution of peridotites from the ocean/continent transition of the Iberia Abyssal Plain margin, *Proceedings of ODP,* **149,** 397–412.

Bevington, P., 1969. *Data Reduction and Error Analysisfor the Physical Sciences,* **Vol. 13,** pp. 985–993, McGraw-Hill, New York.

Boillot, G. & Froitzheim, N., 2001. Non-volcanic rifted margins, continental break-up and the onset of sea-floor spreading: some outstanding questions, *Geol. Soc. Lond. Spec. Publ.,* **187**(1), 9–30.

Boillot, G., Fraud, G., Recq, M. & Girardeau, J., 1989. Undercrusting by serpentinite beneath rifted margins., *Nature,* **341,** 523–525.

Bott, W.F., Smith, B.A., Oakes, G., Sikander, A.H. & Ibrahim, A.I., 1992. The tectonic framework and regional hydrocarbon, prospectivity of the Gulf of Aden, *J. Petrol. Geol.,* **15,** 211–243.

Bown, J. & White, R., 1994. Variation with spreading rate of oceanic crustal thickness and geochemistry, *Earth; planet. Sci. lett.,* **121**(3-4), 435–449.

Brannan, J., Gerdes, K. & Newth, I., 1997. Tectono-stratigraphic development of the Qamar basin, eastern Yemen, *Mar. Pet. Geol.,* **14**(6), 701–730.

Brun, J. & Beslier, M., 1996. Mantle exhumation at passive margins, *Earth planet. Sci. Lett.,* **142**(1-2), 161–173.

Buck, W., 2004. Consequences of athenospheric variability on continental rifting, in *Rheology and Deformation of the Lithosphere at continental margins,* **Vol. 62,** pp. 1–30, eds Karner, G., Taylor, B., Driscoll, N. & Kohlstedt, D., Columbia University Press, New York, NY.

Bullock, A. & Minshull, T., 2005. From continental extension to seafloor spreading: crustal structure of the Goban Spur rifted margin, southwest of the UK, *Geophys. J. Int.,* **163**(2), 527–546.

Cannat, M., 1993. Emplacement of mantle rocks in the seafloor at mid-ocean ridges., *J. geophys. Res.,* **98**(B3), 4163–4172.

Cannat, M. *et al.*, 1995. Thin crust, ultramafic exposures, and rugged faulting patterns at the Mid-Atlantic Ridge (22–24 N), *Geology,* **23**(1), **49**.

Carlson, R. & Raskin, G., 1984. Density of the ocean crust, *Nature,* **311,** 555–558.

Chian, D., Louden, K. & Reid, I., 1995. Crustal structure of the Labrador Sea conjugate margin and implications for the formation of nonvolcanic continental margins, *J. geophys. Res.,* **100**(B12), 24 239–24 254.

Christeson, G., 1995. *OBSTOOL: Software for Processing UTIG OBS Data*, Technical Report, Vol. 134, University of Texas Institute for Geophysics, pp. 1–27.

Contrucci, I., Klingelhofer, F., Perrot, J., Bartolome, R., Gutscher, M., Sahabi, M., Malod, J. & Rehault, J., 2004. The crustal structure of the NW Moroccan continental margin from wide-angle and reflection seismic data, *Geophys. J. Int.,* **159**(1), 117–128.

Davis, M. & Kusznir, N., 2004. Depth-dependent lithospheric stretching at rifted continental margins, in *Proceedings of NSF Rifted Margins Theoretical Institute*. Columbia University Press, New York, pp. 92–136.

Davison, I., 1997. Wide and narrow margins of the Brazilian South Atlantic, *J. Geol. Soc.,* **154**(3), 471–476.

Dean, S., Minshull, T., Whitmarsh, R. & Louden, K., 2000. Deep structure of the ocean-continent transition in the southern Iberia Abyssal Plain from seismic refraction profiles- The IAM-9 transect at 40 deg 20 min N, *J. geophys. Res.,* **105**(B3), 5859–5885.

d'Acremont, E., Leroy, S., Beslier Marie, O., Bellahsen, N., Fournier, M., Robin, C., Maia, M. & Gente, P., 2005. Structure and evolution of the eastern Gulf of Aden conjugate margins from seismic reflection data., *Geophys. J. Int.,* **160**(3), 869–890.

d'Acremont, E., Leroy, S., Maia, M., Patriat, P., Beslier Marie, O., Bellahsen, N., Fournier, M. & Gente, P., 2006. Structure and evolution of the eastern Gulf of Aden; insights from magnetic and gravity data (Encens-Sheba MD117 cruise), *Geophys. J. Int.,* **165**(3), 786–803.

d'Acremont, E., Leroy, S., Maia, M., Gente, P. & Autin, J., 2010. Volcanism, jump and propagation on the Sheba Ridge, eastern Gulf of Aden: segmentation evolution and implications for accretion processes, *Geophys. J. Int.,* **180,** 535–551.

Ebinger, C. & Sleep, N., 1998. Cenozoic magmatism throughout east Africa resulting from impact of a single plume, *Nature,* **395**(6704), 788.

Eldholm, O. & Grue, K., 1994. North Atlantic volcanic margins: dimensions and production rates, *J. geophys. Res.,* **99**(B2), 2955–2968.

Fernàndez, M., Torne, M., Garcia-Castellanos, D., Vergés, J., Wheeler, W. & Karpuz, R., 2004. Deep structure of the Vøring Margin: the transition from a continental shield to a young oceanic lithosphere, *Earth planet. Sci. Lett.,* **221**(1-4), 131–144.

Fournier, M., Patriat, P. & Leroy, S., 2001. Reappraisal of the Arabia–India–Somalia triple junction kinematics, *Earth planet. Sci. Lett.,* **189**(3-4), **103–114**.

Funck, T., Hopper John, R., Larsen Hans, C., Louden Keith, E., Tucholke Brian, E. & Holbrook, W.S., 2003. Crustal structure of the ocean-continent transition at Flemish Cap; seismic refraction results., *J. geophys. Res.,* **108**(B11), 20 pages.

Funck, T., Jackson, H., Louden, K., Dehler, S. & Wu, Y., 2004. Crustal structure of the northern Nova Scotia rifted continental margin (eastern Canada), *J. geophys. Res.,* **109**(B9), B09102.

Funck, T., Andersen, M., Neish, J. & Dahl-Jensen, T., 2008. A refraction seismic transect from the Faroe Islands to the Hatton-Rockall Basin, *J. geophys. Res.,* **113**, B12405, doi:10.1029/2004JB003008.

Gaviglio, P., 1989. Longitudinal waves propagation in a limestone: the relationship between velocity and density, *Rock Mech. Rock Eng.,* **22**(4), 299–306.

Geoffroy, L., 2005. Volcanic passive margins, *C.R.-Géosci.,* **337**(16), 1395–1408.

Greenroyd, C., Peirce, C., Rodger, M., Watts, A. & Hobbs, R., 2008. Demerara Plateau-the structure and evolution of a transform passive margin, *Geophys. J. Int.,* **172**(2), 549–564.

Gregg, P., Lin, J., Behn, M. & Montési, L., 2007. Spreading rate dependence of gravity anomalies along oceanic transform faults, *Nature,* **448**(7150), 183–187.

Hébert, H., Deplus, C., Audin, L., Khanbari, K. & Huchon, P., 2001. Lithospheric structure of a nascent spreading ridge inferred from gravity data- The western Gulf of Aden, *J. geophys. Res.,* **106**(B11), 26 345–26 364.

Hirsch, K., Bauer, K. & Scheck-Wenderoth, M., 2009. Deep structure of the western South African passive margin Results of a combined approach of seismic, gravity and isostatic investigations, *Tectonophysics,* **470**(1-2), **57–70**.

Hofmann, C., Courtillot, V., Feraud, G., Rochette, P., Yirgu, G., Ketefo, E. & Pik, R., 1997. Timing of the Ethiopian flood basalt event and implications for plume birth and global change, *Nature,* **389**(6653), 838–841.

Holbrook, W., Purdy, G., Sheridan, R., Glover, L., III, Talwani, M., Ewing, J. & Hutchinson, D., 1994a. Seismic structure of the US Mid-Atlantic continental margin, *J. geophys. Res,* **99**(17), 871–17.

Holbrook, W., Reiter, E., Purdy, G., Sawyer, D., Stoffa, P., Austin, J., Oh, J. & Makris, J., 1994b. Deep structure of the US Atlantic continental margin, offshore South Carolina, from coincident ocean bottom and multichannel seismic data, *J. geophys. Res.,* **99**(B5), 9155–9178.

Holbrook, W. *et al.*, 2001. Mantle thermal structure and active upwelling during continental breakup in the North Atlantic, *Earth planet. Sci. Lett.,* **190**(3-4), 251–266.

Hopper, J. & Buck, W., 1996. The effect of lower crustal flow on continental extension and passive margin formation, *J. geophys. Res.,* **101,** 20–20.

Hopper, J., Dahl-Jensen, T., Holbrook, W., Larsen, H., Lizarralde, D., Korenaga, J., Kent, G. & Kelemen, P., 2003. Structure of the SE Greenland margin from seismic reflection and refraction data: implications for nascent spreading center subsidence and asymmetric crustal accretion during North Atlantic opening, *J. geophys. Res,* **108,** 2269.

Horen, H., Zamora, M. & Dubuisson, G., 1996. Seismic wave velocities and anisotropy in serpentinized periodotites from Xigaze ophiolite: abudance of serpentine in slow spreading ridge, *Geophys. Res. lett.,* **23**(1), 9–12.

Horsefield, S., Whitmarsh, K., White, R. & Sibuet, J., 1994. Crustal structure of the Goban Spur rifted continental margin, Ne Atlantic, *Geophys. J. Int.,* **119**(1), 1–19.

Huismans, R. & Beaumont, C., 2008. Complex rifted continental margins explained by dynamical models of depth-dependent lithospheric extension, *Geology,* **36**(2), 163.

Jestin, F., Huchon, P. & Gaulier, J., 1994. The Somalia plate and the East African Rift System: present-day kinematics, *Geophys. J. Int.,* **116**(3), 637–654.

Keen, C., 1987. Some important consequences of lithospheric extension, *Geol. Soc. Lond. Spec. Publ.,* **28**(1), 67–73.

Kenea, N., Ebinger, C. & Rex, D., 2001. Late Oligocene volcanism and extension in the southern Red Sea hills, *Sudan: J. Geol. Soc. Lond.,* **158,** 285–294.

Klingelhoefer, F., Minshull, T., Blackman, D., Harben, P. & Childers, V., 2001. Crustal structure of Ascension Island from wide-angle seismic data: implications for the formation of near-ridge volcanic islands, *Earth planet. Sci. Lett.,* **190**(1-2), 41–56.

Klingelhoefer, F. *et al.*, 2009. Crustal structure of the SW-Moroccan margin from wide-angle and reflection seismic data (the DAKHLA experiment) Part A: wide-angle seismic models, *Tectonophysics,* **468**(1-4), 63–82.

Kusznir, N. & Park, R., 1987. The extensional strength of the continental lithosphere: its dependence on geothermal gradient, and crustal composition and thickness, *Geol. Soc. Lond. Special Publ.,* **28**(1), 35–52.

Lau, K., Louden, K., Funck, T., Tucholke, B., Holbrook, W., Hopper, J. & Larsen, H., 2006. Crustal structure across the Grand Banks–Newfoundland Basin Continental Margin–I. Results from a seismic refraction profile, *Geophys. J. Int.,* **167**(1), 127–156.

Lavier, L. & Manatschal, G., 2006. A mechanism to thin the continental lithosphere at magma-poor margins., *Nature,* **440**(7082), 324–328.

Leroy, S. *et al.*, 2004. From rifting to spreading in the eastern Gulf of Aden; a geophysical survey of a young oceanic basin from margin to margin., *Terra Nova,* **16**(4), 185–192.

Leroy, S., Ebinger, C., d'Acremont, E., Stuart, G., Al-Lazki, A., Tiberi, C., Autin, J., Watremez, L., Beslier, M., Bellahsen, N. & Encens-team, 2006. The onshore-offshore ENCENS project: Imaging the stretching/thinning of the continental lithosphere and inception of oceanic spreading in the eastern Gulf of Aden, *EOS, Trans. AGU,* 2006 Fall Meeting, abstract #T53A-1567.

Leroy, S., d'Acremont, E., Tiberi, C., Basuyau, C., Autin, J., Lucazeau, F. & Sloan, H., 2010a. Recent off-axis volcanism in the eastern Gulf of Aden: implications for plume-ridge interaction, *Earth planet. Sci. Lett.,* **293,** 140–153.

Leroy, S. *et al.*, 2010b. Contrasted styles of rifting in the eastern Gulf of Aden: A combined wide-angle, multichannel seismic, and heat flow survey, *Geochem. Geophys. Geosyst.,* **11,** Q07004.

Lizarralde, D., Holbrook, W., McGeary, S., Bangs, N. & Diebold, J., 2002. Crustal construction of a volcanic arc, wide-angle seismic results from the western Alaska Peninsula, *J. geophys. Res.,* **107**(B 8), 4–21.

Lucazeau, F. *et al.*, 2008. Persistent thermal activity at the Eastern Gulf of Aden after continental break-up, *Nature Geosciences,* **1,** 854–858.

Lucazeau, F. *et al.*, 2009. Post-rift volcanism and high heat-flow at the Ocean-Continent Transition of the Gulf of Aden, *Terra Nova,* **21,** 285–292.

Ludwig, W., Nafe, J. & Drake, C., 1970. Seismic refraction, *The Sea,* **4**(Part 1), 53–84.

Menzies, M., Klemperer, S., Ebinger, C. & Baker, J., 2002. Characteristics of volcanic rifted margins, *Volcanic Rifted Margins,* **362,** 1–14.

Minshull, T., 2009. Geophysical characterisation of the ocean–continent transition at magma-poor rifted margins, *C.R.-Géosci.,* **341**(5), 382–393.

Minshull, T., Lane, C., Collier, J. & Whitmarsh, R., 2008. The relationship between rifting and magmatism in the northeastern Arabian Sea, *Nat. Geosci.,* **1**(7), 463–467.

Mjelde, R., Raum, T., Myhren, B., Shimamura, H., Murai, Y., Takanami, T., Karpuz, R. & Naess, U., 2005. Continent-ocean transition on the Vøring Plateau, NE Atlantic, derived from densely sampled ocean bottom seismometer data., *J. geophys. Res.,* **110**, B05101, doi:10.1029/2004JB003026.

Mjelde, R., Raum, T., Murai, Y. & Takanami, T., 2007. Continent-ocean-transitions: Review, and a new tectono-magmatic model of the Vøring Plateau, NE Atlantic., *J. Geodyn.,* **43**(3), 374–392.

Morgan, J., Barton, P. & White, R., 1989. The Hatton Bank continental margin. III: structure from wide-angle OBS and multichannel seismic refraction profiles, *Geophys. J. Int.,* **98**(2), 367–384.

Mutter, J., Talwani, M. & Stoffa, P., 1982. Origin of seaward-dipping reflectors in oceanic crust off the Norwegian margin by 'subaerial sea-floor spreading, *Geology,* **10**(7), 353–357.

Mutter, J., Buck, W. & Zehnder, C., 1988. Convective partial melting, 1. A model for the formation of thick basaltic sequences during the initiation of spreading, *J. geophys. Res,* **93,** 1031–1048.

Pérez-Gussinyé M. & Reston, T., 2001. Rheological evolution during extension at nonvolcanic rifted margins: onset of serpentinization and development of detachments leading to continental breakup, *J. geophys. Res.,* **106**(B3), 3961–3976.

Pérez-Gussinyé, M., Ranero, C., Reston, T. & Sawyer, D., 2003. Mechanisms of extension at nonvolcanic margins: evidence from the Galicia interior basin, west of Iberia, *J. geophys. Res,* **108,** 2245, doi:10.1029/2001JB000901.

Péron-Pinvidic, G. & Manatschal, G., 2009. The final rifting evolution at deep magma-poor passive margins from Iberia-Newfoundland: a new point of view, *Int. J. Earth Sci.,* **98**(7), 1581–1597.

Planke, S., Alvestad, E. & Eldholm, O., 1999. Seismic characteristics of basaltic extrusive and intrusive rocks, *Leading Edge,* **18**(3), 342–348.

Raum, T. *et al.*, 2002. Crustal structure of the southern part of the Vøring Basin, mid-Norway margin, from wide-angle seismic and gravity data, *Tectonophysics,* **355**(1-4), 99–126.

Reid, I., 1994. Crustal structure of a nonvolcanic rifted margin east of Newfoundland, *J. geophys. Res,* **99**(B8), 15 161–15 180.

Reston, T., 2007. Extension discrepancy at North Atlantic nonvolcanic rifted margins: depth-dependent stretching or unrecognized faulting? *Geology,* **35**(4), 367–370.

Reston, T., 2009. The structure, evolution and symmetry of the magma-poor rifted margins of the North and Central Atlantic: a synthesis., *Tectonophysics,* **468**(1-4), 6–27.

Rodriguez, E., Morris, C., Belz, J., Chapin, E., Martin, J., Daffer, W. & Hensley, S., 2005. An assessment of the SRTM topographic products, Tech. rep., Jet Propulsion Laboratory., Pasadena, California.

Roger, J., Platel, J. & Cavelier, C., 1989. Données nouvelles sur la stratigraphie et lhistoire géologique du Dhofar (Sultanat dOman), *Bull. Soc. Geol. Fr,* **2,** 265–277.

Rommevaux, C., Deplus, C., Patriat, P. & Sempere, J., 1994. Three-dimensional gravity study of the Mid-Atlantic Ridge: Evolution of the segmentation between 28 deg and 29 deg N during the last 10 my, *J. geophys. Res,* **99**(B2), 3015–3029.

Salisbury, M. & Christensen, N., 1978. The seismic velocity structure of a traverse through the Bay of Islands ophiolite complex, Newfoundland, an exposure of oceanic crust and upper mantle, *J. geophys. Res,* **83,** 805–817.

Sandwell, D. & Smith, W., 1997. Marine gravity anomaly from Geosat and ERS 1 satellite altimetry, *J. geophys. Res,* **102**(10), 10 039–10 054.

Schroeder, T., John, B. & Frost, B., 2002. Geologic implications of seawater circulation through peridotite exposed at slow-spreading mid-ocean ridges, *Geology,* **30**(4), 367–370.

Stockwell, J., 1997. Free software in education; a case study of CWP/SU; Seismic Un*x, *The Leading Edge,* **16**, 1045–1049.

Talwani, M., Lamar Worzel, J. & Landisman, M., 1959. Rapid Gravity Computations for Two-Dimensional Bodies with Application to the Mendocino Submarine Fracture Zone, *J. geophys. Res.,* **64,** 49–59.

Tard, F., Masse, P., Walgenwitz, F. & Gruneisen, P., 1991. The volcanic passive margin in the vicinity of Aden, Yemen, *Bulletin des centres de recherches exploration-production Elf Aquitaine, Boussens,* **15,** 1–9.

Tiberi, C., Leroy, S., d'Acremont, E., Bellahsen, N., Ebinger, C., Al Lazki, A. & Pointu, A., 2007. Crustal geometry of the northeastern Gulf of Aden passive margin; localization of the deformation inferred from receiver function analysis, *Geophys. J. Int.,* **168**(3), 1247–1260.

Van Avendonk, H., Lavier, L., Shillington, D. & Manatschal, G., 2009. Extension of continental crust at the margin of the eastern Grand Banks, Newfoundland, *Tectonophysics,* **468**(1-4), 131–148.

Veevers, J. & Cotterill, D., 1978. Western margin of Australia: Evolution of a rifted arch system., *Geol. Soc. Am. Bull.,* **89**(3), 337–355.

Vigny, C., Huchon, P., Ruegg, J., Khanbari, K. & Asfaw, L., 2006. Confirmation of Arabia slow plate motion by new GPS data in Yemen, *J. geophys. Res,* **111**, B02402, doi:10.1029/2004JB003229.

Watchorn, F., Nichols, G. & Bosence, D., 1998. Rift-related sedimentation and stratigraphy, southern Yemen (Gulf of Aden), in *Sedimentation and Tectonics in Rift Basins: Red Sea–Gulf of Aden.,* pp. 165–189, Chapman & Hall, London.

Wernicke, B., 1985. Uniform-sense normal simple shear of the continental lithosphere, *Can. J. Earth Sci.,* **22**(1), 108–125.

Wessel, P. & Smith, W.H.L., 1995. New version of the Generic Mapping Tools released, *EOS, Trans. AGU,* **76**, 329.

White, R. & McKenzie, D., 1989. Magmatism at Rifts zones: the generation of volcanic continental margin and flood basalts, *J. geophys. Res.,* **94**(1), 7685–7730.

White, R., Spence, G., Fowler, S., McKenzie, D., Westbrook, G. & Bowen, A., 1987. Magmatism at rifted continental margins, *Nature(London),* **330**(6147), 439–444.

White, R., McKenzie, D. & O'Nions, R., 1992. Oceanic crustal thickness from seismic measurements and rare earth element inversions, *J. geophys. Res.,* **97**(B13), 19 683–19 715.

Zelt, C. & Forsyth, D., 1994. Modeling wide-angle seismic data for crustal structure: southeastern Grenville Province, *J. geophys. Res.,* **99**(B6), 11 687–11 704.

Zelt, C.A., 1999. Modelling strategies and model assessment for wide-angle seismic traveltime data, *Geophys. J. Int.,* **139,** 183–204.

Zelt, C.A. & Smith, R.B., 1992. Seismic traveltime inversion for 2-D crustal velocity structure, *Geophys. J. Int.,* **108,** 16–34.

APPENDIX A: FURTHER MODELLING STATISTICS AND DATA FITTING

The deep structure along the Ashawq–Salalah segment has been constrained by more than 19 000 rays traced in six velocity models. This allow us to distinguish up to 11 wide-angle seismic phases, from the direct waves in the water to the refracted waves in the upper-mantle. The modelling statistics for each of these phases and for each line is shown in the Table A1, and all the fits for each line are shown in the Fig. A1.

Table A1. Modelling statistics for each wide-angle seismic phase for each line (*N*, traveltimes number).

	Lines across to the strike								
		ENCR01			ENCR02			ENCR04	
Phase	*N*	RMS (s)	χ^2	*N*	RMS (s)	χ^2	*N*	RMS (s)	χ^2
WW	98	0.035	3.030	301	0.033	2.471	164	0.056	1.276
sed_{2R}	64	0.053	0.726	26	0.047	0.145			
sed_2	7	0.049	7.054	89	0.045	1.644			
bas_R	53	0.053	1.365				58	0.040	0.350
P_{g1}	557	0.167	2.046	658	0.050	0.368	235	0.037	1.963
P_gP							104	0.068	1.988
P_{g2}	481	0.109	1.440	1328	0.099	0.637	977	0.058	3.263
P_mP /P_tP	490	0.170	1.861	1096	0.209	2.804	176	0.067	0.584
P_b				585	0.079	0.489	604	0.076	3.315
P_bP				238	0.085	0.460	149	0.073	0.486
P_n	228	0.076	0.770	780	0.191	2.334	26	0.037	0.092
All	1978	0.137	1.703	5101	0.142	1.358	2493	0.063	2.509

	Lines along the strike								
		ENCR05			ENCR07			ENCR09	
Phase	*N*	RMS (s)	χ^2	*N*	RMS (s)	χ^2	*N*	RMS (s)	χ^2
WW	228	0.052	5.513	326	0.045	0.829	449	0.043	2.209
bas_R	82	0.036	0.252	165	0.070	1.013	149	0.048	0.704
P_{g1}	352	0.040	0.656	137	0.054	0.594	182	0.084	7.452
P_gP	115	0.044	0.278						
P_{g2}	981	0.037	0.514	1303	0.096	1.150	1986	0.112	4.158
P_mP /P_tP	274	0.044	0.243	136	0.197	3.915	267	0.114	1.726
P_b	403	0.049	0.358						
P_bP	203	0.067	0.313						
P_n				726	0.114	1.082	1140	0.168	3.042
All	2638	0.045	0.876	2469	0.107	1.245	4173	0.123	3.504

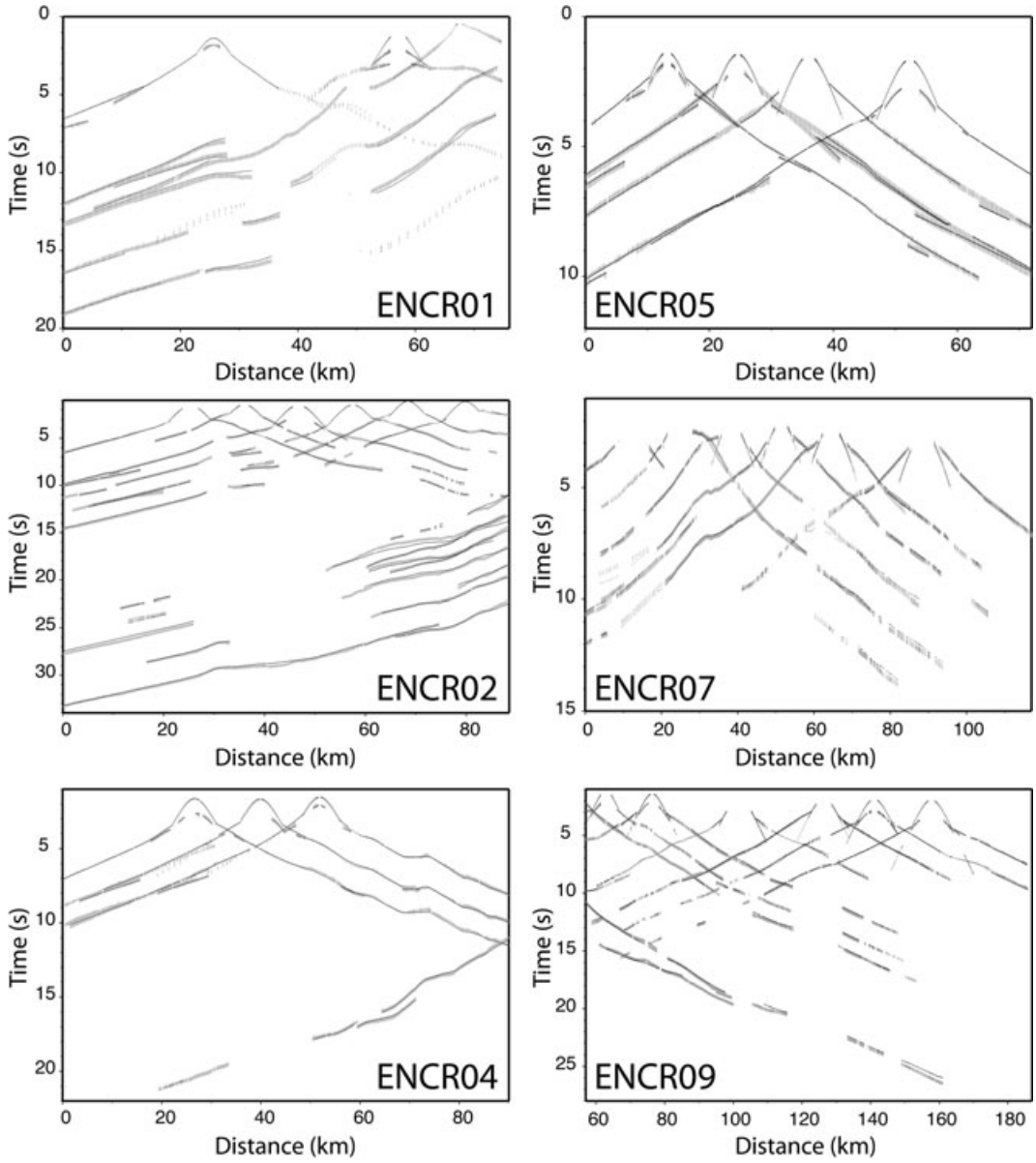

Figure A1. Picks with variable uncertainties (grey bars) and synthetic traveltimes (black dots) for each profile of this study.